The Astrophysical Journal, 810:10 (18pp), 2015 September 1 doi:10.1088/0004-637X/810/1/10


# THE DISK-OUTFLOW SYSTEM IN THE S255IR AREA OF HIGH-MASS STAR FORMATION

I. Zinchenko[1,2], S.-Y. Liu[3], Y.-N. Su[3], S. V. Salii[4], A. M. Sobolev[4], P. Zemlyanukha[1,2], H. Beuther[5], D. K. Ojha[6], M. R. Samal[7], and Y. Wang[8,9]

[1] Institute of Applied Physics of the Russian Academy of Sciences, 46 Ulyanov st., Nizhny Novgorod 603950, Russia
[2] Lobachevsky State University of Nizhni Novgorod, 23 Gagarin av., Nizhny Novgorod 603950, Russia; zin@appl.sci-nnov.ru
[3] Institute of Astronomy and Astrophysics, Academia Sinica, P.O. Box 23-141, Taipei 10617, Taiwan, R.O.C.
[4] Ural Federal University, Ekaterinburg, Russia
[5] Max-Planck-Institut für Astronomie, Heidelberg, Germany
[6] Infrared Astronomy Group, Department of Astronomy and Astrophysics, Tata Institute of Fundamental Research, Homi Bhabha Road, Colaba, Mumbai (Bombay)–400 005, India
[7] Laboratoire d'Astrophysique de Marseille (UMR 6110 CNRS & Université de Provence), 38 rue F. Joliot-Curie, F-13388 Marseille Cedex 13, France
[8] Department of Astronomy, University of Geneva, Switzerland
[9] Purple Mountain Observatory, CAS, China

*Received 2015 April 16; accepted 2015 July 17; published 2015 August 24*

## ABSTRACT

We report the results of our observations of the S255IR area with the Submillimeter Array (SMA) at 1.3 mm in the very extended configuration and at 0.8 mm in the compact configuration as well as with the IRAM 30 m at 0.8 mm. The best achieved angular resolution is about 0.4 arcsec. The dust continuum emission and several tens of molecular spectral lines are observed. The majority of the lines is detected only toward the S255IR-SMA1 clump, which represents a rotating structure (probably a disk) around the young massive star. The achieved angular resolution is still insufficient to make any conclusions about the Keplerian or non-Keplerian character of the rotation. The temperature of the molecular gas reaches 130–180 K. The size of the clump is about 500 AU. The clump is strongly fragmented as follows from the low beam-filling factor. The mass of the hot gas is significantly lower than the mass of the central star. A strong DCN emission near the center of the hot core most probably indicates a presence of a relatively cold ($\lesssim$80 K) and rather massive clump there. High-velocity emission is observed in the CO line as well as in lines of high-density tracers HCN, $HCO^+$, CS and other molecules. The outflow morphology obtained from a combination of the SMA and IRAM 30 m data is significantly different from that derived from the SMA data alone. The CO emission detected with the SMA traces only one boundary of the outflow. The outflow is most probably driven by jet bow shocks created by episodic ejections from the center. We detected a dense high velocity clump associated apparently with one of the bow shocks. The outflow strongly affects the chemical composition of the surrounding medium.

*Key words:* astrochemistry – HII regions – instrumentation: interferometers – ISM: clouds – ISM: molecules – stars: formation

## 1. INTRODUCTION

The formation of high mass stars (more massive than 8–10 $M_\odot$) is still poorly understood. Studies of this process are currently a "hot topic" of astrophysical research. A major unsolved problem of high-mass star formation is the characterization of accretion disks around young high-mass protostars. To date, most of evidence for the existence of such disks has been indirect (e.g., Beuther et al. 2009). If present, these disks undoubtedly play a crucial role in the star formation process. Nevertheless, the very existence of these disks, much less their physical properties, is not well-established. The importance of understanding these disks cannot be understated. For example, because of the larger masses involved, it is quite possible that high-mass disks are self-gravitating, unlike their Keplerian low-mass counterparts, implying that there may be significant dynamical differences between the high-mass and low-mass star formation processes.

S255IR is a part of the well known massive star-forming complex located between the evolved Sharpless H II regions S255 and S257. Several authors have estimated the photometric distance to the complex at about 2.5 kpc (Russeil et al. 2007; Chavarría et al. 2008; Ojha et al. 2011). However, Rygl et al. (2010) report a distance of 1.6 kpc based on trigonometric parallax measurements of methanol masers. This seems to be the most accurate distance estimate and we adopt it here, too. The previous studies have shown that S255IR contains a cluster of early B-type stars (Howard et al. 1997; Itoh et al. 2001), several compact H II regions (Snell & Bally 1986), and a number of $H_2$ emission features (Miralles et al. 1997). The total mass of the S255IR core has been estimated from single-dish observations at $M \sim 300$–$400\,M_\odot$ (Zinchenko et al. 2009; Wang et al. 2011). The estimate of the luminosity has been $L \sim 2 \times 10^4\,L_\odot$ (Wang et al. 2011).

The interferometric observations by Wang et al. (2011) revealed three continuum clumps and a high-velocity collimated outflow in the S255IR area. Our Paper I (Zinchenko et al. 2012) was devoted to the general structure and kinematics of the complex based on the Submillimeter Array (SMA) observations at 1.3 and 1.1 mm (the synthesized beam sizes were approximately $3\farcs8 \times 3\farcs0$ at 1.3 mm and $2\farcs9 \times 2\farcs6$ at 1.1 mm) as well as VLA ammonia observations and GMRT low frequency continuum data. Our results as well as data by Wang et al. (2011) indicate in particular a presence of a hot rotating core and a spectacular outflow in the S255IR region. However, the angular resolution was insufficient for a more detailed investigation of this core. In addition, a reliable evaluation of physical and chemical properties of this system

required observations of additional molecular transitions. Therefore we performed observations of the S255IR area with the SMA at a much higher angular resolution and at higher frequencies.

Here we present observational data for S255IR obtained at 1.3 mm with the SMA in the very extended configuration and at 0.8 mm in the compact configuration. In addition we observed this area with the IRAM 30 m radio telescope in order to obtain short-spacing data complementing the SMA results. We mainly discuss properties of the dense cores and high velocity outflows observed in this area.

## 2. OBSERVATIONS AND DATA REDUCTION

### 2.1. SMA

The S255IR area was observed with the SMA in its compact configuration on 2010 December 14 at 350 GHz. A three-field mosaic was obtained with the following phase centers: $06^h12^m53\overset{s}{.}800$, $17°59'22\overset{''}{.}1$, $06^h12^m54\overset{s}{.}8876$, $17°59'29\overset{''}{.}3353$, and $06^h12^m52\overset{s}{.}7124$, $17°59'14\overset{''}{.}8647$. The primary HPBW of the SMA antennas is 36″ at these frequencies. Typical system temperatures on source were between 200 and 400 K. The resulting *uv* coverage ranges from 10 to 90 k$\lambda$ (8 antennas in the array). 3C454.3 and Uranus were used as the bandpass calibrators and 0532+075, 0750+125, and 0530+135 were used as the complex phase and amplitude gain calibrators. A total of 8 GHz (342−346 GHz in the LSB and 354−358 GHz in the USB) was observed with the SMA bandwidth doubling correlator configuration. The spectral resolution was 0.8125 MHz.

In addition on 2011 January 07 S255IR was observed in the very extended configuration at 225 GHz. A single field was observed with the same phase center as for the central field at 350 GHz. The primary HPBW of the SMA antennas is 55″ at these frequencies. Typical system temperatures on source were between 90 and 200 K. The resulting *uv* coverage ranges from 50 k$\lambda$ to 350 k$\lambda$ (7 antennas in the array). 3C454.3 and 3C279 were used as the bandpass calibrators and 0750+125 and 0530+135 were used as the complex phase and amplitude gain calibrators. A total of 8 GHz (217.0−220.8 GHz in the LSB and 229.1−232.95 GHz in the USB) was observed with the SMA bandwidth doubling correlator configuration. The spectral resolution was 0.406 and 1.625 MHz (given the limited correlator capability, we were not able to have a high resolution across the whole band, so we assigned different resolutions to different tracers). These data were combined with our previous data obtained at the same frequencies in the compact configuration (Paper I) which enables an investigation of the source structure in a wider range of spatial scales.

The gain calibrator flux scale, calibrated against Uranus at 350 GHz and Callisto at 225 GHz, was found to be consistent within 5% with the SMA calibrator database and estimated to be accurate within 20%.

The data calibration was carried out with the IDL superset MIR (Scoville et al. 1993), and subsequent imaging and analysis were done in MIRIAD (Sault et al. 1995). With robust weighting for the continuum and line data, the synthesized beam sizes are approximately $2\overset{''}{.}2 \times 1\overset{''}{.}9$ at 350 GHz and $0\overset{''}{.}5 \times 0\overset{''}{.}4$ at 225 GHz. The rms noise is approximately 7 mJy beam$^{-1}$ and 1 mJy beam$^{-1}$ in the continuum images at 350 GHz and 225 GHz, respectively, and 100 mJy beam$^{-1}$ and 20 mJy beam$^{-1}$ in the spectral cubes at these frequencies at 2 km s$^{-1}$ resolution.

### 2.2. IRAM 30 m Radio Telescope

Single-dish observations of several molecular lines at the 30 m IRAM radio telescope were performed in 2012 October ($N_2H^+$ $J = 3$–2 at 279.5 GHz), 2012 December (SiO $J = 5$-4 at 217.1 GHz), and 2014 January (CO $J = 3$–2 at 345.8 GHz and CS $J = 7$–6 at 342.9 GHz). The antenna HPBW was $9\overset{''}{.}3$, $11\overset{''}{.}9$ and $7\overset{''}{.}5$ at these frequencies, respectively. The observations were performed in the OTF mode with position switching using the HERA receiver at 217.1 GHz and EMIR receiver at higher frequencies. The central position of the maps was the same as for the primary field in the SMA observations. The reference position was selected at −500″ in right ascension from the central position. Apparently a weak CO(3–2) emission is present at the reference position resulting in a weak negative feature in the CO spectra at $V_{LSR} \approx 24$ km s$^{-1}$ (the bulk of the line emission in this area is observed at $V_{LSR} \sim 4$–10 km s$^{-1}$). This feature does not affect significantly the observed spectra. The system temperature was ∼200 K for the $N_2H^+$ observations, ∼300 K for the SiO observations and ∼600 K for the CO and CS observations. Pointing was checked regularly on nearby strong sources and pointing errors were within a few arcseconds. The antenna temperature calibration was made by the standard chopper-wheel method.

The map size was approximately $2\overset{'}{.}0 \times 2\overset{'}{.}5$ for the $N_2H^+$ and SiO observations, covering both S255IR and S255N regions, and approximately $1\overset{'}{.}5 \times 1\overset{'}{.}0$ for the CO and CS observations, covering only the S255IR area. Here we discuss only the data relevant to S255IR. The data on S255N are postponed to further publications.

The data reduction was performed with the GILDAS package (http://www.iram.fr/IRAMFR/GILDAS). Then the single-dish data were combined with the SMA data using the MIRIAD procedures as described by, e.g., Wang et al. (2011). The conversion to the flux density scale was made using the conversion factors presented on the IRAM 30 m telescope website.

## 3. OBSERVATIONAL RESULTS AND DATA ANALYSIS

With the SMA we detected several tens of spectral lines in both 350 and 225 GHz bands. A list of these lines, including their frequencies and energy of lower levels, is given in Tables 1, 2. The spectral line parameters are taken from the JPL (Pickett et al. 1998) and CDMS (Müller et al. 2001, 2005) catalogs.

We present the results in the form of maps as well as spectra and line parameters at selected positions. For continuum observations we give positions, flux densities, and size estimates of the continuum sources.

### 3.1. Data Analysis

#### 3.1.1. Methanol

For the methanol data analysis, we constructed simple radiative transfer model, which uses the large velocity gradient (LVG) approximation. Dust emission and absorption within the emission region was taken into account in the way described by Sutton et al. (2004). We assumed that the dust particles are intermixed with gas. The same physical temperature for the gas

**Table 1**
List of Molecular Transitions Observed at the SMA in the Very Extended Configuration in S255IR

| Molecule | Transition | Frequency (GHz) | $E_l$ (K) |
|---|---|---|---|
| $^{12}$CO | 2–1 | 230.538000 | 5.532 |
| $^{13}$CO | 2–1 | 220.398684 | 5.289 |
| $CH_3OH$ | $6_1$–$7_2$ A$^-$ | 217.299202 | 363.496 |
| | $15_6$–$16_5$ A$^-$ | 217.642677 | 735.160 |
| | $15_6$–$16_5$ A$^+$ | 217.642678 | 735.160 |
| | $20_1$–$20_0$ E | 217.886504 | 497.919 |
| | $4_2$–$3_1$ E | 218.440063 | 34.976 |
| | $8_0$–$7_1$ E | 220.078561 | 86.051 |
| | $15_4$–$16_3$ E | 229.589056 | 363.420 |
| | $8_{-1}$–$7_0$ E | 229.758756 | 78.076 |
| | $19_5$–$20_4$ A$^+$ | 229.864121 | 567.565 |
| | $19_5$–$20_4$ A$^-$ | 229.939095 | 567.561 |
| | $3_{-2}$–$4_{-1}$ E | 230.027047 | 28.788 |
| | $22_2$–$21_{-3}$ E | 230.292196 | 598.499 |
| | $10_2$–$9_3$ A$^-$ | 231.281110 | 154.248 |
| | $10_2$–$9_3$ A$^+$ | 232.418521 | 154.248 |
| | $18_3$–$17_4$ A$^+$ | 232.783446 | 435.360 |
| $^{13}$CS | 5–4 | 231.220686 | 22.194 |
| DCN | 3–2 | 217.238530 | 10.425 |
| HNCO | $10_{0,10}$–$9_{0,9}$ | 219.798282 | 47.471 |
| | $10_{1,9}$–$9_{1,8}$ | 220.584762 | 90.916 |
| | $10_{1,10}$–$9_{1,9}$ | 218.981170 | 90.569 |
| | $10_{2,9}$–$9_{2,8}$ | 219.733850 | 217.739 |
| | $10_{2,8}$–$9_{2,7}$ | 219.737193 | 217.739 |
| | $10_{3,8}$–$9_{3,7}$ | 219.656770 | 422.417 |
| | $10_{3,7}$–$9_{3,6}$ | 219.656771 | 422.417 |
| $HC_3N$ | 24–23 | 218.324711 | 120.504 |
| SO | $6_5$–$5_4$ | 219.949433 | 24.429 |
| $H_2CO$ | $3_{0,3}$–$2_{0,2}$ | 218.222195 | 10.483 |
| | $3_{2,2}$–$2_{2,1}$ | 218.475642 | 57.608 |
| | $3_{2,1}$–$2_{2,0}$ | 218.760071 | 57.613 |
| OCS | 18–17 | 218.903357 | 89.304 |
| | 19–18 | 231.060983 | 99.810 |
| HCOOH | $10_{0,10}$–$9_{0,9}$ | 220.038072 | 48.061 |
| | $10_{1,9}$–$9_{1,8}$ | 231.505705 | 53.355 |
| $CH_3CN$ | $12_6$–$11_6$ | 220.594423 | 315.313 |
| | $12_5$–$11_5$ | 220.641084 | 236.810 |
| | $12_4$–$11_4$ | 220.679287 | 172.555 |
| | $12_3$–$11_3$ | 220.709017 | 122.565 |
| | $12_2$–$11_2$ | 220.730261 | 86.849 |
| | $12_1$–$11_1$ | 220.743011 | 65.416 |
| | $12_0$–$11_0$ | 220.747261 | 58.272 |

**Table 2**
List of Molecular Transitions Observed at the SMA in the Compact Configuration in S255IR

| Molecule | Transition | Frequency (GHz) | $E_l$ (K) |
|---|---|---|---|
| $^{12}$CO | 3–2 | 345.795990 | 16.596 |
| CS | 7–6 | 342.882850 | 49.372 |
| $HCO^+$ | 4–3 | 356.734242 | 25.682 |
| $CH_3OH$ | $13_1$–$13_0$ A$^{-+}$ | 342.729796 | 211.024 |
| | $13_{-1}$–$14_{-2}$ E | 343.599019 | 607.550 |
| | $18_2$–$17_3$ E | 344.109039 | 402.884 |
| | $19_1$–$18_2$ A$^+$ | 344.443433 | 434.697 |
| | $16_1$–$15_2$ A$^-$ | 345.903916 | 316.049 |
| | $18_{-3}$–$17_{-4}$ E | 345.919260 | 442.829 |
| | $13_0$–$12_1$ A$^+$ | 355.602945 | 193.959 |
| HCN | 4–3 | 354.505473 | 25.251 |
| | 4–3 (0,1$^{1c}$,0) | 354.460435 | 1049.892 |
| | 4–3 (0,1$^{1d}$,0) | 356.255568 | 1050.021 |
| H$^{13}$CN | 4–3 | 345.339769 | 24.861 |
| HC$^{15}$N | 4–3 | 344.200109 | 24.779 |
| $HC_3N$ | 38–37 | 345.609016 | 306.905 |
| | 39–38 | 354.697456 | 323.492 |
| SO | $8_8$ – $7_7$ | 344.310792 | 70.957 |
| $^{33}$SO | $8_{9,8}$–$7_{8,7}$ | 343.086102 | 61.564 |
| | $8_{9,9}$–$7_{8,8}$ | 343.087298 | 61.566 |
| $SO_2$ | $13_{2,12}$–$12_{1,11}$ | 345.338538 | 76.410 |
| | $12_{4,8}$–$12_{3,9}$ | 355.045517 | 93.960 |
| | $13_{4,10}$–$13_{3,11}$ | 357.165390 | 105.823 |
| | $15_{4,12}$–$15_{3,13}$ | 357.241193 | 132.537 |
| | $11_{4,8}$–$11_{3,9}$ | 357.387580 | 82.800 |
| | $8_{4,4}$–$8_{3,5}$ | 357.581449 | 55.202 |
| | $9_{4,6}$–$9_{3,7}$ | 357.671821 | 15.992 |
| | $7_{4,4}$–$7_{3,5}$ | 357.892442 | 47.835 |
| | $6_{4,2}$–$6_{3,3}$ | 357.925848 | 41.402 |
| | $17_{4,14}$–$17_{3,15}$ | 357.962905 | 162.932 |
| $H_2CS$ | $10_{0,10}$–$9_{0,9}$ | 342.946424 | 74.132 |
| | $10_{2,9}$–$9_{2,8}$ | 343.322082 | 126.830 |
| | $10_{3,8}$–$9_{3,7}$ | 343.409963 | 192.613 |
| | $10_{3,7}$–$9_{3,6}$ | 343.414146 | 192.556 |
| HCOOH | $16_{1,16}$–$15_{1,15}$ | 342.521225 | 127.153 |
| | $15_{1,14}$–$14_{1,13}$ | 343.952413 | 119.774 |
| | $16_{0,16}$–$15_{0,15}$ | 345.030596 | 126.494 |
| | $16_{2,15}$–$15_{2,14}$ | 356.137250 | 141.578 |

and dust components is assumed. The molecular emission region was assumed to be spherically symmetric and uniform in $H_2$ density, gas and dust temperature, gas-to-dust ratio, and methanol fractional abundance. The influence of external infrared sources was not considered. The dust opacity law was chosen as $\tau_{\rm dust} \propto \lambda^{-2}$. We adopted a gas-to-dust mass ratio of 100 and a cross section at 1 mm of $2.6 \times 10^{-25}$ cm$^2$ (Sherwood et al. 1980). In addition to the model described in Sutton et al. (2004) we used the collision transition rates based on the model of collisions of methanol molecules with He and para-$H_2$ molecules (Cragg et al. 2005). The scheme of energy levels in this model includes rotational levels with quantum numbers $J$ up to 22, $|K|$ up to 9; the levels include the rotational levels of the ground, first, and second torsionally excited states. In total, 861 levels of A-methanol and 852 levels of E-methanol were considered according to Cragg et al. (2005).

With this model we made estimates of the hydrogen number density, $n_{\rm H_2}$, specific column density of methanol, $N_{\rm CH_3OH}/\Delta V$, gas kinetic temperature, $T_{\rm kin}$, and fractional abundance of methanol $N_{\rm CH_3OH}/N_{\rm H_2}$, using the measured values of "quasi-thermal" (i.e., non-maser) methanol lines. The variable parameter of the source size is introduced in order to take into account beam-dilution effects.

The brightness temperatures of all detected "quasi-thermal" methanol lines as well as upper limits for the brightness temperatures of other lines were taken into account.

We have searched for a set of parameters that provides the best agreement between the values of the calculated brightness temperatures ($T_i^{\rm mod}$) and the measured brightness temperatures ($T_i^{\rm obs}$). This corresponds to the minimum of $\chi^2 = \sum_i^N ((T_i^{\rm obs} - T_i^{\rm mod})/\sigma_i)^2$, where $\sigma_i$ is observational uncertainty for a particular line.

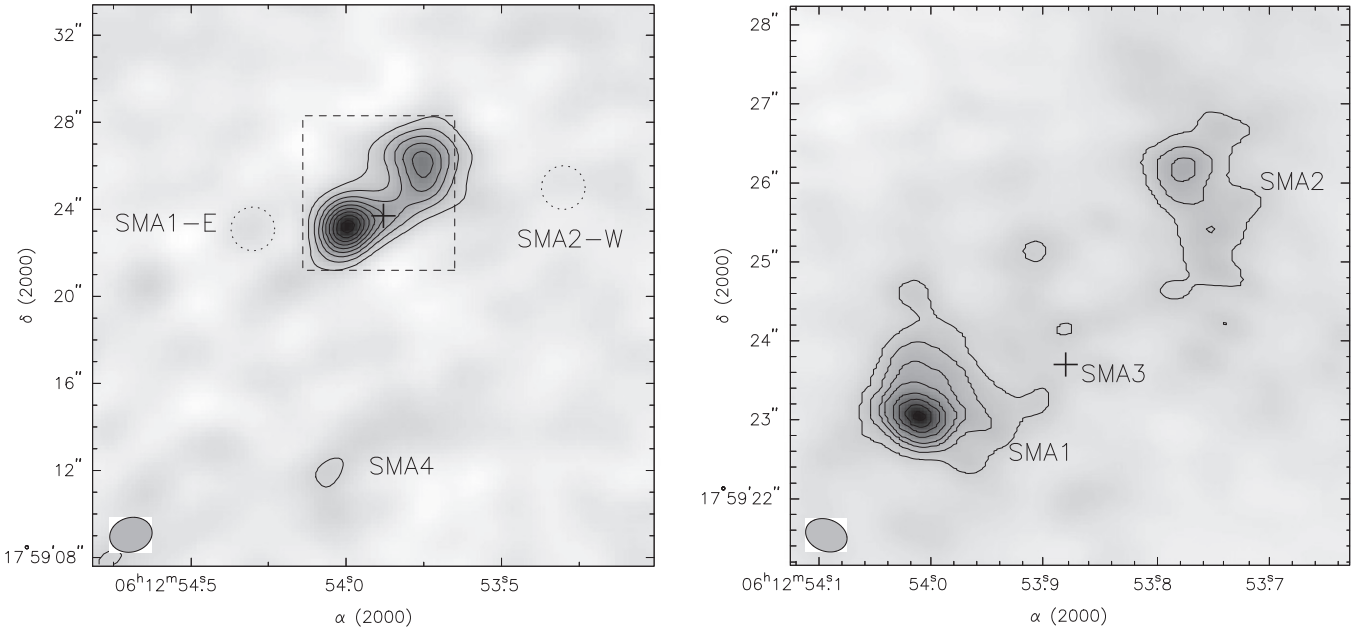


**Figure 1.** Left panel: map of the 0.8 mm continuum emission in the S255IR. The contour levels are (1, 2, 3, 4, 5, 6, 7, 8, 9, 10) × 40 mJy beam$^{-1}$. The dashed rectangle indicates the area shown in the right panel. The dotted circles indicate positions of two molecular clumps discussed in the text. Right panel: map of the 1.3 mm continuum emission in the S255IR. The contour levels are (2, 3, 4, 5, 7, 9, 11, 13) × 4 mJy beam$^{-1}$. The SMA beam is shown in the lower left corner of both panels. The crosses mark the position of the SMA3 clump according to Wang et al. (2011).

The sources appear inhomogeneous in some cases. However, the LVG approximation treats the problem locally and does not actually require physical homogeneity of the source. It can be well used for an inhomogeneous medium (e.g., Ossenkopf 1997). We have chosen the simplest approximation for the case of the source which is smaller than the beam—we introduced the filling factor which is equal to the portion of the source size in the beam. The value of the filling factor is well constrained because the model is sensitive to its changes. We do not have enough observational constraints to study real clumpiness of the source. Introducing additional poorly constrained parameters will reduce validity of the modeling.

#### 3.1.2. Methyl Cyanide

Methyl cyanide ($CH_3CN$) is a symmetric-top molecule which is an efficient "thermometer" for dense molecular gas (e.g., Boucher et al. 1980). To derive the kinetic temperature we used the population diagram analysis which takes into account the optical depth in the $CH_3CN$ lines and the beam filling factor as described by Wang et al. (2010).

### 3.2. Millimeter Wave Continuum

Maps of the continuum emission at 0.8 and 1.3 mm are presented in Figure 1. The 1.3 mm map was obtained by combining our new measurements in the very extended configuration with the previous measurements in the compact configuration (Paper I). It shows a rather extended emission and compact cores in the SMA1 and SMA2 clumps.

Estimates of the continuum source parameters are given in Tables 3, 4. For the measurements at 1.3 mm we indicate the parameters of the compact cores seen in the very extended configuration. Parameters of the more extended components were presented in Paper I. The measured fluxes are several hundreds mJy at 350 GHz and several tens mJy at 225 GHz in the very extended configuration. The deconvolved sizes are from ∼1 arcsec to a few arcseconds at 345 GHz and about 0.3 arcsec for the compact cores at 225 GHz.

**Table 3**
Names, Positions, Flux Densities, Deconvolved Angular Sizes, and Position Angles of the Millimeter Wave Continuum Sources Measured at 350 GHz in the Compact Configuration

| Name | $\alpha$(2000) (h m s) | $\delta$(2000) (° ′ ″) | $S_{350}$ (Jy) | $\theta_{max}$ (″) | $\theta_{min}$ (″) | P.A. (°) |
|---|---|---|---|---|---|---|
| S255IR-SMA1 | 6:12:54.00 | 17:59:23.2 | 0.50 | 1.4 | 0.6 | −11 |
| S255IR-SMA2 | 6:12:53.76 | 17:59:26.1 | 0.56 | 2.4 | 2.1 | 4 |
| S255IR-SMA3 | 6:12:53.86 | 17:59:23.7 | 0.13 | 1.3 | 0.3 | 44 |
| S255IR-SMA4 | 6:12:54.01 | 17:59:12.0 | 0.25 | 5.9 | 3.8 | −82 |

**Table 4**
Names, Positions, Flux Densities, Deconvolved Angular Sizes, and Position Angles of the Millimeter Wave Continuum Sources Measured at 225 GHz in the Very Extended Configuration

| Name | $\alpha$(2000) (h m s) | $\delta$(2000) (° ′ ″) | $S_{225}$ (Jy) | $\theta_{max}$ (″) | $\theta_{min}$ (″) | P.A. (°) |
|---|---|---|---|---|---|---|
| S255IR-SMA1 | 6:12:54.010 | 17:59:23.06 | 0.058 | 0.30 | 0.27 | −19 |
| S255IR-SMA2 | 6:12:53.779 | 17:59:26.16 | 0.016 | 0.49 | 0.31 | −27 |

### 3.3. Basic Properties of the Molecular Emission

Here we give the general description of the observed molecular emission. More detailed information on the relevant species and transitions is presented in the following sections.

The general morphology and kinematics of the molecular emission were described in Paper I. Our new data set contains several tens of molecular transitions. In Figure 2 we present representative maps obtained with the SMA at 0.8 mm.

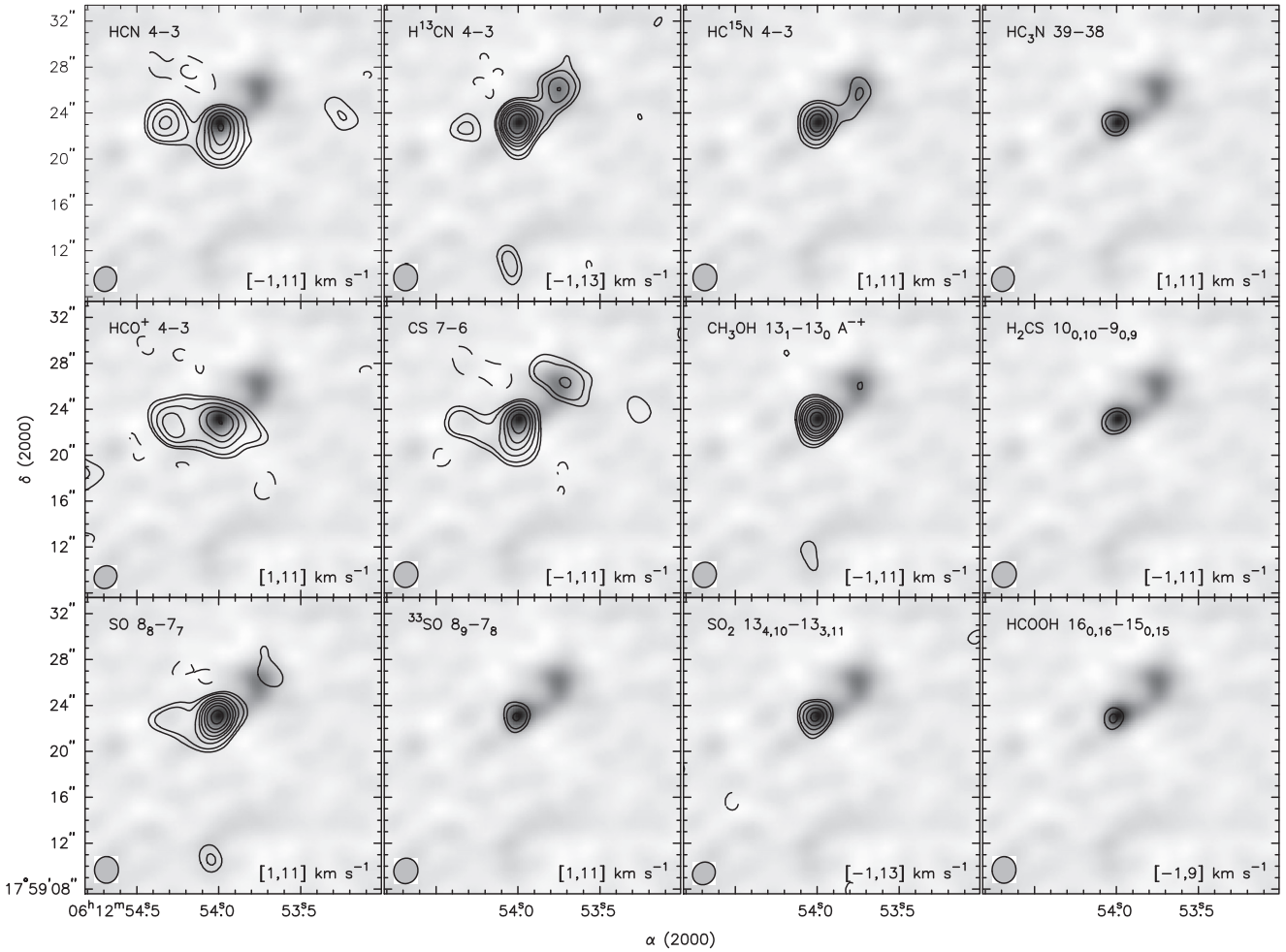


**Figure 2.** Maps of the integrated line emission for several representative transitions of various molecules (contours) overlaid on the image of the 0.8 mm continuum emission. The velocity interval is shown at the bottom of each panel. The dashed contours show negative features due to the missing flux. The contour levels are the following: $(-3, -2, 2, 3, 5, 7, 9, 12, 15, 20) \times A$ Jy beam$^{-1}$ km s$^{-1}$, where $A = 3$ for HCN and $HCO^+$, $A = 1$ for $H^{13}CN$, $HC^{15}N$, $HC_3N$, $H_2CS$, $CH_3OH$, $^{33}SO$, $SO_2$, and HCOOH, $A = 2$ for CS, and $A = 1.5$ for SO. The SMA beam is shown in the lower left corner of each panel.

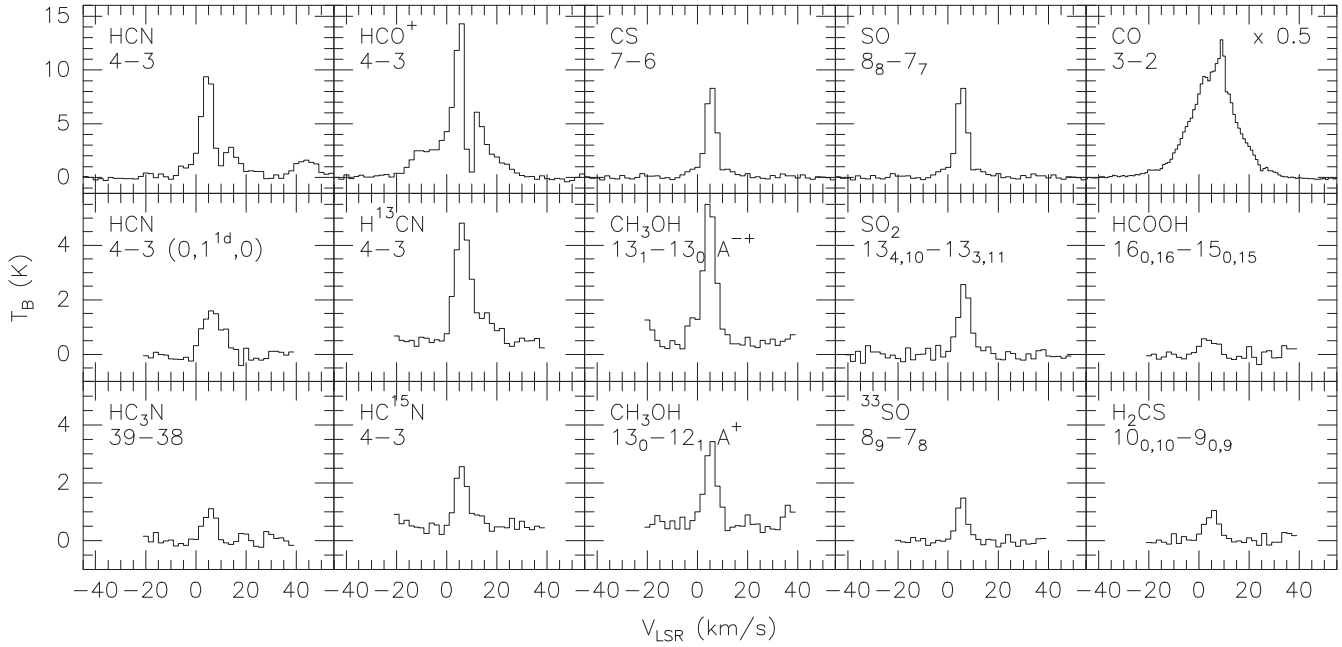


**Figure 3.** Spectra of several representative molecular transitions toward the SMA1 clump. The CO(3–2) spectrum is scaled by a factor of 0.5. It is obtained from the combined SMA and IRAM 30 m data. The other spectra are from the SMA data only. The angular resolution is about 2 arcsec.

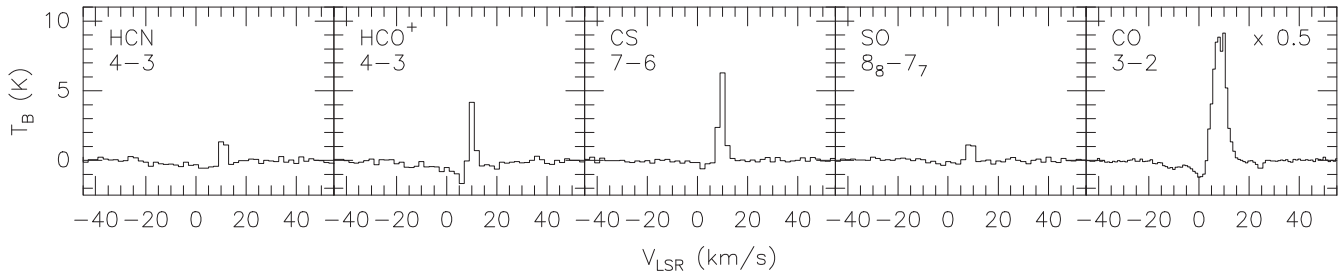


**Figure 4.** Spectra of several representative molecular transitions toward the SMA2 clump. The CO(3–2) spectrum is scaled by a factor of 0.5. It is obtained from the combined SMA and IRAM 30 m data. The other spectra are from the SMA data only. The angular resolution is about 2 arcsec.

These maps confirm that SMA1 is the brightest source of molecular emission in this area. High-excitation lines are observed exclusively toward this clump. Several lower excitation molecular lines are detected also in SMA2. Emission of HCN, SO, and $CH_3OH$ is also observed in SMA4. HCN and CS emission is probably present in the area to the west of SMA2, designated as S255IR-$N_2H^+$(1) in Paper I. Since it is observed not in $N_2H^+$ only and for simplicity we shall designate it hereafter as SMA2-W.

A new feature, not noticed in our Paper I and in other previous works is a molecular clump to the east of SMA1 with a rather strong emission in the HCN, $HCO^+$, CS and SO lines (Figure 2). We shall designate it as SMA1-E. This clump is located near the head of the jet observed in the NIR emission (see below).

Spectra of several representative transitions toward the SMA1 and SMA2 clumps are presented in Figures 3, 4.

As mentioned in Paper I the main emission peak toward the SMA1 clump is at $V_{LSR}$ ∼4–5 km s$^{-1}$. The line width is $\gtrsim$5 km s$^{-1}$. Several lines including CO, HCN, $HCO^+$, CS, and SO show broad wings indicative of high-velocity outflow. We discuss this feature in the following sections. A rather strong emission is detected from vibrationally excited HCN with an excitation energy ∼1000 K above the ground level.

The line emission from the SMA1-E clump peaks at about 8 km s$^{-1}$. The line width is large, ∼5 km s$^{-1}$.

The emission from the SMA2 clump is observed at about 10 km s$^{-1}$. The lines are narrow, ∼2 km s$^{-1}$.

With the very extended array we detected line emission almost exclusively from the SMA1 compact core. No emission was detected in $C^{18}O$ and SiO indicating an absence of compact structures in the lines of these molecules. The results of these observations are presented and discussed below.

## 4. STRUCTURE, KINEMATICS, AND PHYSICAL PROPERTIES OF DENSE CORES

Our data presented in Paper I and here as well as data by Wang et al. (2011) indicate the presence of four continuum clumps in the S255IR area, designated S255IR-SMA1 to S255IR-SMA4. In addition, in Paper I we detected clumps with a rather strong molecular emission without continuum counterparts in the SMA data. One of them, S255IR-$N_2H^+$(1), is located close to SMA2 and was observed in the $N_2H^+$, $NH_3$, and several $CH_3OH$ lines. Estimates of their basic physical properties were presented in Paper I. Here we further investigate these objects using the new data set.

### 4.1. SMA1

SMA1 is the brightest object in this area. As shown in Section 3 most of the observed molecular lines are detected only here. The deconvolved size of the continuum source at 350 GHz measured with the SMA in the compact configuration (Table 3) is close to that found in Paper I. The flux density measured at 350 GHz is only slightly higher than the flux density obtained at 284 GHz (Paper I). It is worth noting that in Paper I we could not separate the SMA1 and SMA3 clumps. However, even if we take the integrated flux of these clumps at 350 GHz, the spectral index in the range 284–350 GHz will be only 1.6 which is inconsistent with a presumably optically thin dust emission at these frequencies. Most probably this implies a significantly larger flux loss at 350 GHz in comparison with the measurements at 284 GHz due to a smaller beam size.

The deconvolved size of the continuum source detected with the SMA in the very extended configuration is about 0.″3 (Table 4) which corresponds to about 500 AU. The observed aspect ratio for this core is close to unity.

#### 4.1.1. Kinematics

Wang et al. (2011) noticed rotation of the core around the axis roughly parallel to the outflow direction. Now, at subarcsecond resolution we can investigate the core kinematics on smaller scales. In Figure 5 we present maps of the first moment of the $CH_3OH$ emission in the $4_2$–$3_1$ E line and $CH_3CN$ emission in the $12_3$–$11_3$ line. In this figure we also indicate the axis of the jet previously identified through IR observations (Howard et al. 1997) and locations of the water masers measured with the VLBA (Goddi et al. 2007).

This figure clearly shows that the core is really rotating around the axis of the jet. The rotation velocities along the line of sight amount to a few km s$^{-1}$ (it varies from about 3 km s$^{-1}$ to about 7 km s$^{-1}$ for $CH_3OH$ $4_2$–$3_1$ E and to about 8 km s$^{-1}$ for $CH_3CN$ $12_3$–$11_3$). In Figure 6 we present the position–velocity diagram for the $CH_3OH$ emission in the $4_2$–$3_1$ E line along the cut through the core center perpendicular to the jet axis (P.A. = 157°). It clearly shows the velocity gradient which can be consistent with Keplerian rotation but the angular resolution is still insufficient for firm conclusions about the character of this rotation.

An implicit indication of a probable further increase of the rotation velocity in the innermost part of the core comes from the line width map (Figure 7). It shows a significant increase of

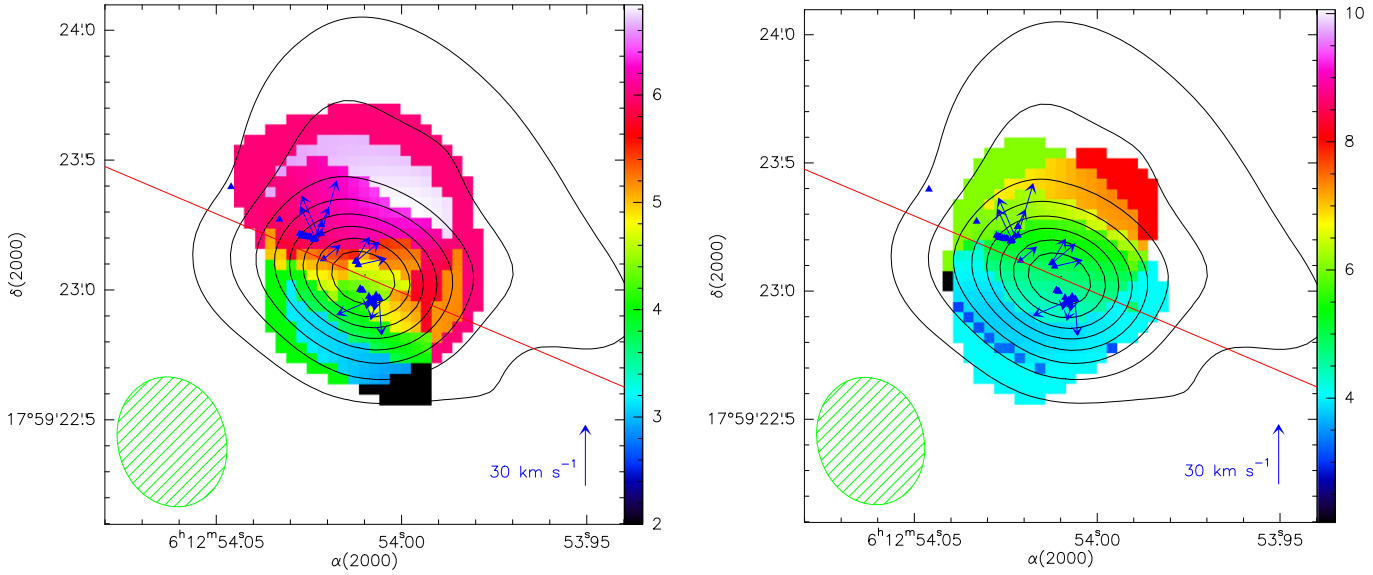


**Figure 5.** Maps of the first moment of the $CH_3OH$ emission in the $4_2$–$3_1$ E line (left panel, color scale) and $CH_3CN$ emission in the $12_3$–$11_3$ line (right panel, color scale) toward the SMA1 clump. The intensity cut-off is 100 mJy beam$^{-1}$ km s$^{-1}$ for $CH_3OH$ and 200 mJy beam$^{-1}$ km s$^{-1}$ for $CH_3CN$. Contours show the 1.3 mm continuum emission. The triangles mark water masers (Goddi et al. 2007) and the arrows indicate their proper motions (in the cases when they are measured). The red line indicates the jet axis as found by Howard et al. (1997). The beam for the molecular maps is shown in the lower left corner of both panels. The scale for the velocities of the proper motions is shown in the lower right corner. The pixels with the lowest velocities appear as the blue squares in the right panel.

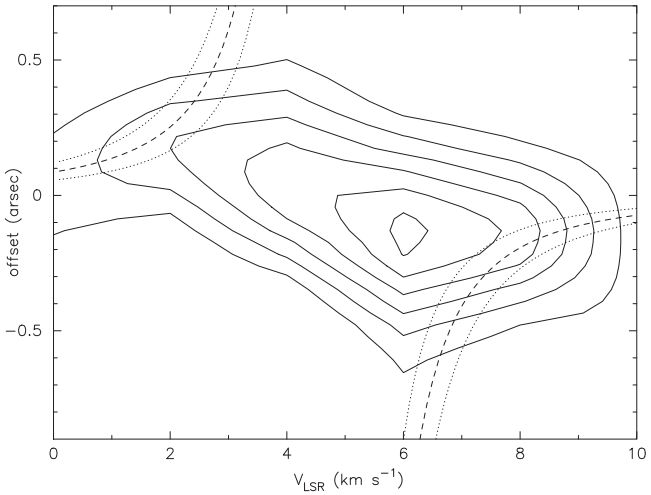


**Figure 6.** Position–velocity diagram for the $CH_3OH$ emission in the $4_2$–$3_1$ E line along the cut through the SMA1 center perpendicular to the jet axis (P.A. = 157°). The dashed curves correspond to Keplerian rotation around a central mass of 20 $M_\odot$ with an inclination angle of 25°, and the dotted curves correspond to the inclination angles of 25° ± 5°.

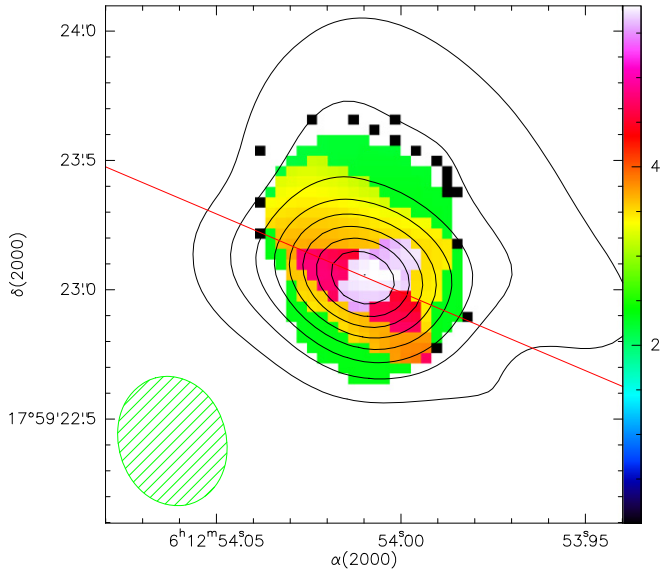


**Figure 7.** Map of the second moment of the $CH_3OH$ emission in the $4_2$–$3_1$ E line (color scale). Contours show the 1.3 mm continuum emission. The beam for the molecular map is shown in the lower left corner.

the line width in the center which can be related to rotation (the line width increases from about 2 km s$^{-1}$ at the periphery to about 6 km s$^{-1}$ in the center).

It is also worth mentioning an increased line width along the jet axis (Figure 7). It can be probably explained by an increased turbulence caused by the passage of the jet.

The $HCO^+$(4–3) and probably HCN(4–3) spectra toward SMA1 (Figure 3) show the redshifted absorption dip which may be suggestive of infall. The CO(3–2) spectrum measured with the SMA has a similar (although broader) feature (Figure 8). At the same time the CO(3–2) spectrum obtained from the combined SMA and IRAM 30 m data shows a peak at these velocities. Most probably it means that this feature is related to an extended component resolved out by the SMA, although an infall cannot be fully excluded.

#### 4.1.2. Physical Properties

Let us consider physical parameters of this core. We estimated gas kinetic temperature from the $CH_3CN$ and $CH_3OH$ observations. Modeling of the $CH_3CN$ emission (Figure 9) as described in Section 3.1.2 yields a kinetic temperature in the range (74.9–197.6) K ($1\sigma$ confidence interval) toward the emission peak (Table 5). We have detected a large number (15) of $CH_3OH$ transitions toward SMA1 (Table 1). From the $CH_3OH$ analysis (Section 3.1.1) we obtain $T_{\rm kin}$ = 178 K with the 165–195 K $1\sigma$

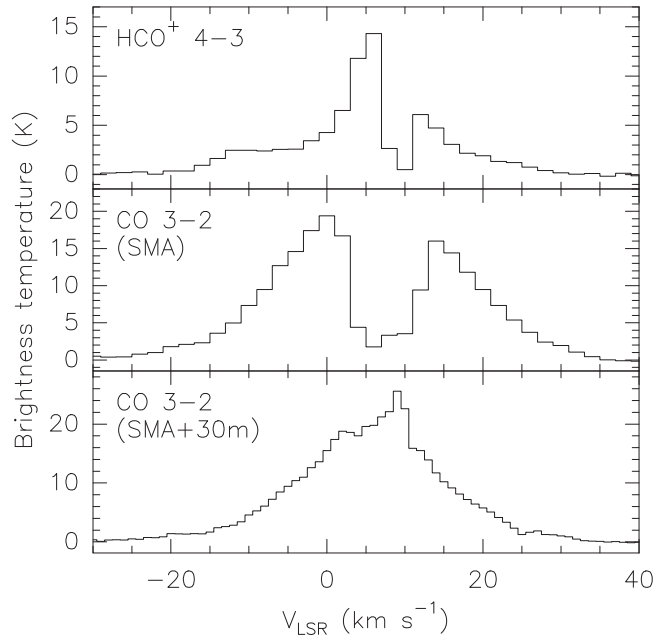


**Figure 8.** SMA spectra of $HCO^+$(4–3) and CO(3–2) as well as the combined SMA+30 m spectrum of CO(3–2) toward SMA1. The angular resolution is about 2 arcsec.

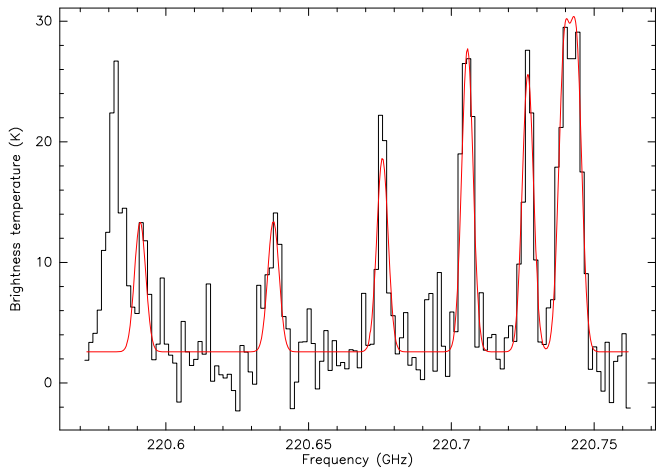


**Figure 9.** $CH_3CN$ spectrum measured toward the SMA1 emission peak and the model fit.

**Table 5**
Kinetic Temperature, $CH_3CN$ Column Density, Beam Filling Factor, and Line Optical Depth Derived from the $CH_3CN$ Data Obtained in the Very Extended Configuration (HPBW ≈0.″4) at the Central Position in SMA1

| Parameter | Fit results |
|---|---|
| $T_{kin}$ (K) | 128.8 (74.9–197.6) |
| $N_L(CH_3CN)$ ($10^{16}$ cm$^{-2}$) | 2.12 (0.96–5.80) |
| Beam filling factor | 0.23 (0.18–0.36) |
| $\tau(K=0)$ | 2.53 (0.93–8.37) |

**Note.** The 1$\sigma$ confidence intervals are indicated in parentheses.

confidence interval at the center, $T_{kin}$ = 170–200 K at 0.″2 to the north, and $T_{kin}$ = 140–165 K at 0.″2 to the south (Table 6). Therefore there is probably a temperature gradient in the north–south direction. The temperature seems to be anti-correlated with the $CH_3OH$ column density (Table 6, Figure 10).

We adopt the gas kinetic temperature of 170 K as the average value (it is close to the weighted average of the $CH_3OH$ and $CH_3CN$ results). Assuming the same temperature (170 K) for the dust we obtain a total mass of this hot component of about 0.3 $M_\odot$. As in Paper I we assume a gas-to-dust mass ratio of 100 and adopt a dust absorption efficiency following Ossenkopf & Henning (1994). The peak gas column density estimated from the continuum data is $N(H_2) \sim 3 \times 10^{24}$ cm$^{-2}$. With a size of 500 AU the mean density of hot gas is about $6 \times 10^8$ cm$^{-3}$. This is two times higher than our estimate of the SMA1 mean density in Paper I taking into account the difference in the adopted distances here and in Paper I. This increase can be expected since now we consider much smaller scales near the core center. The $CH_3OH$ modeling puts no significant constraints on density. The relative abundance of $CH_3OH$ is $\sim 10^{-6}$.

Both $CH_3CN$ and $CH_3OH$ observations indicate a beam filling factor of 0.15–0.2. This means that the source is very inhomogeneous on the 0.″4 scale and probably consists of clumps with a size of ≪500 AU and a density much higher than the mean density found above. This higher density estimate does not contradict the $CH_3OH$ data. A similar picture of clumpy medium was inferred from our observations of high-mass star-forming regions on larger scales (Pirogov & Zinchenko 2008; Pirogov et al. 2012). Most probably it reflects turbulence in the cores.

Our data set includes several other tracers of the hot gas. One of the most important is HNCO. We detected HNCO lines in different $K_{-1}$ ladders ($K_{-1}$ = 0, 1, 2, 3) with excitation energies up to ∼400 K (Table 1). In Figure 11 we present the rotational diagram for the observed HNCO transitions. This diagram was obtained from peak integrated line intensities found by 2D Gaussian fitting of the integrated intensity maps in different HNCO lines. We used the line strengths and dipole moment from the Cologne Database for Molecular Spectroscopy (Müller et al. 2001, 2005).

This diagram indicates a rotational temperature of 318 ± 70 K (Table 7). However, the $K_{-1}$ = 0, 1 transitions can be saturated. The peak brightness temperature in these transitions is close to the brightness temperature in the apparently optically thick lines (e.g., CO and $CH_3CN$) and our modeling using RADEX (van der Tak et al. 2007) shows that at the derived physical parameters and column density the optical depth in these lines is about unity. In this case the derived rotational temperature would apparently represent an upper limit to the excitation temperature. The deconvolved source size is ∼0.″3 × 0.″2 for the $K_{-1}$ = 0 transition and decreases for higher $K_{-1}$ ladders. The map of the integrated intensity in the HNCO $K_{-1}$ = 2 transition is shown in Figure 12 along with the map of the OCS emission which is another tracer of hot gas. The peaks of the HNCO and OCS emission practically coincide with the continuum peak, although distributions of these molecules seem to be somewhat different.

The total HNCO column density derived from the rotational diagram is $\sim 2 \times 10^{16}$ cm$^{-2}$. We used the partition function from the Cologne Database for Molecular Spectroscopy (Müller et al. 2001, 2005), too. A comparison with the total gas column density indicates HNCO abundance of $X$(HNCO) ∼ $10^{-8}$. This is a rather high value, close to the highest HNCO abundance derived in the survey of massive cores by Zinchenko et al. (2000). However, taking into account the note above about the HNCO lines saturation, this value may need a correction.

In the 350 GHz band we detected many $SO_2$ lines (Table 2). The corresponding population diagram is shown in Figure 13.

**Table 6**
Physical Parameters Derived from the $CH_3OH$ Data Obtained in the Very Extended Configuration (HPBW ≈0.″4) at Several Positions in SMA1

| Offsets (″, ″) | $T_{kin}$ (K) | $N_{CH_3OH}/\Delta V$ ($10^{12}$ cm$^{-3}$s) | $n_{H_2}$ ($10^8$ cm$^{-3}$) | Beam Filling Factor (%) | $N_{CH_3OH}/N_{H_2}$ |
|---|---|---|---|---|---|
| 0, +0.2 | 183 (170–200) | 3.6 (2.8–5.0) | 3.2 | 14.8 (13.9–16.4) | $10^{-6}$(>$10^{-7}$) |
| 0, 0 | 178 (165–195) | 5.6 (4.0–9.5) | 3.2 | 16.0 (15.2–17.2) | $10^{-6}$(>$10^{-7}$) |
| 0, −0.2 | 153 (140–165) | 8.9 (5.0–12.6) | 0.2 | 15.2 (13.3–16.0) | $10^{-6}$(>$10^{-7}$) |

**Note.** The 1$\sigma$ confidence intervals are indicated in the parentheses (the density $n_{H_2}$ is not constrained by the model as evident from Figure 10).

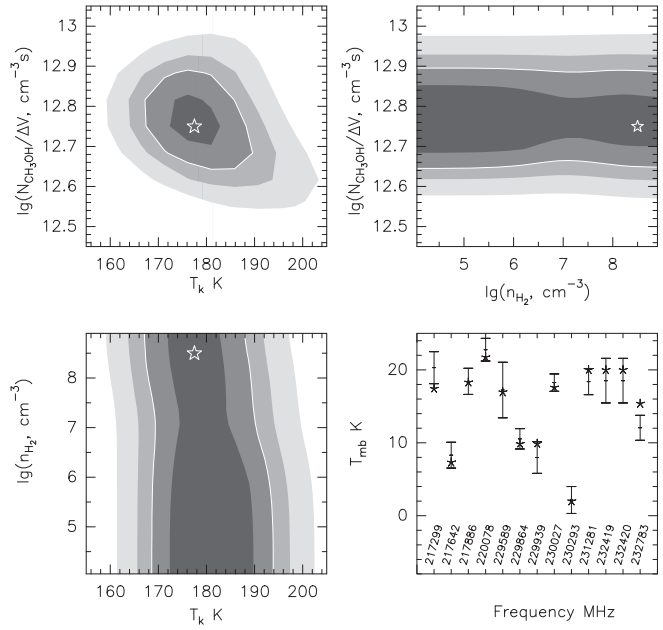


**Figure 10.** Example of the $CH_3OH$ data fitting for the central position in SMA1. Variations of $\chi^2$ with the model parameters are shown in the two top and left bottom panels. The minimum of $\chi^2$ is marked by the star. Confidence intervals of 0.25, 1, 1.6, and 2.6 $\sigma$ are plotted on the gray scale. The confidence interval of 1 $\sigma$ is marked by the white line. A comparison of the model (stars) and observed main-beam temperatures is shown in the right bottom panel.

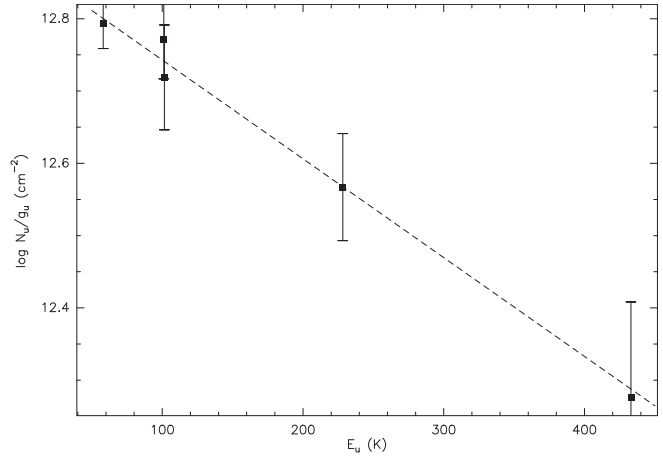


**Figure 11.** Rotational diagram for HNCO toward the emission peak.

It indicates a range of temperatures. For low-excitation transitions the rotational temperature is 65 ± 11 K. For the high-excitation ones it is 146 ± 16 K. The $SO_2$ observations were performed at a much lower angular resolution (2 arcsec) than in the case of HNCO and apparently include emission from both the hot core and the surrounding cloud. The derived temperatures are consistent with the other estimates for these components.

**Table 7**
Fit Results for the Rotational Diagrams Obtained toward SMA1

| Molecule | $T_{kin}$ (K) | log $N_L$ (cm$^{-2}$) | HPBW (″) |
|---|---|---|---|
| HNCO | 318(70) | 16.34(0.04) | ≈0.4 |
| $SO_2$ | 146(16) | 15.50(0.05) | ≈2 |
| | 65(11) | 15.35(0.08) | ≈2 |

**Note.** The 1$\sigma$ uncertainties are indicated in parentheses. In the last column the approximate HPBW for the corresponding data is indicated.

Another indicator of the hot environment is the vibrationally excited HCN. We detected the emission in the $v_2 = 1$ state, about 1000 K above the ground state. For the $v_2 = 2$ emission the upper limit is about five times lower. Following the analysis presented in, e.g., Veach et al. (2013) we obtain an upper limit for the excitation temperature between these states of about 500 K. This is consistent with the other estimates of the gas temperature given above. The critical density for HCN excitation is high (>$10^{10}$ cm$^{-3}$, Veach et al. 2013) which is consistent with our density estimates for the hot gas.

#### 4.1.3. A Cold Clump in the Hot Core?

In Figure 14 we plot maps of the DCN $J = 3$–2 and $^{13}$CS $J = 5$–4 integrated line emission in the SMA1 core. The emission regions are very compact and the emission peak is shifted from the continuum peak which apparently coincides with the YSO location. The projected distance from the continuum peak is roughly 300 AU.

The velocities of the DCN and $^{13}$CS emission are practically the same as those of high excitation lines of other molecules tracing apparently the hot gas. Therefore, most probably the observed DCN emission arises within the disk and since we probably see the disk nearly face-on as discussed above, the physical distance from the center is not much larger than the projected distance. An estimate of the abundances in the LTE approximation gives $X$(DCN) > $10^{-11}$ and $X$($^{13}$CS) > 3 × $10^{-11}$ (assuming the total mass of the clump <10 $M_\odot$ and temperature of 50–100 K). This is a "normal" value for $^{13}$CS while the derived DCN abundance implies a significant deuteration as follows from comparison with typical HCN abundances in massive cores (e.g., Zinchenko et al. 2009). As pointed out in Paper I, recent modeling by Albertsson et al. (2013) shows that the DCN/HCN abundance ratio sharply drops at temperatures ≳80 K. It means that the temperature of the DCN-emitting clump should be rather low, much lower than the temperature of the hot gas in the disk. Another possible explanation, as also discussed in Paper I, could be a very young age of the clump, insufficient to reach the steady-

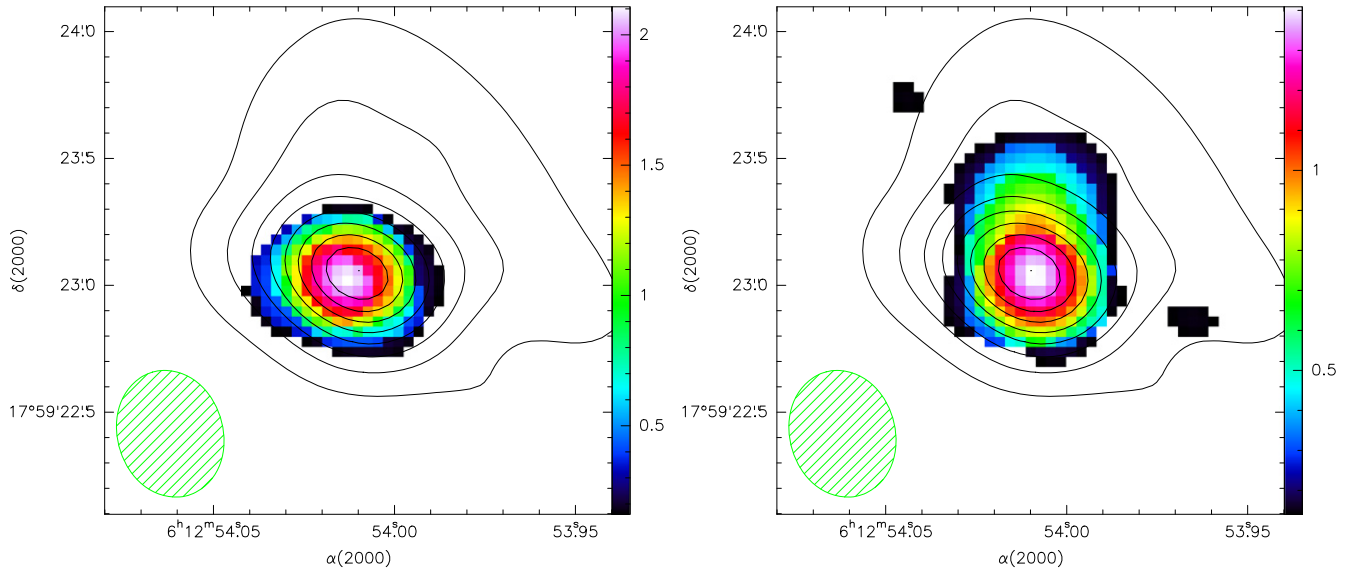


**Figure 12.** Maps of the integrated intensity of HNCO $J_{K_{-1}} = 10_2$–$9_2$ (left panel) and OCS $J = 18$–17 (right panel) transitions (color scale) toward the SMA1 clump. The intensity units are Jy beam$^{-1}$ km s$^{-1}$. The beam size is 0.″4. The contours show the 1.3 mm continuum emission with the same angular resolution. The beam for the molecular maps is shown in the lower left corner of both panels.

**Table 8**
Physical Parameters Derived from the $CH_3OH$ Data Obtained in the Compact Configuration (HPBW ≈3″)

| Object | $T_{kin}$ (K) | $N_{CH_3OH}/\Delta V$ ($10^{12}$ cm$^{-3}$s) | $n_{H_2}$ (cm$^{-3}$) | Beam Filling Factor (%) | $N_{CH_3OH}/N_{H_2}$ |
|---|---|---|---|---|---|
| SMA2 | 50 (40–80) | 2.0 (1.8–3.5) | $6.3 \times 10^6$ ($\leqslant 10^8$) | 99.3 ($\geqslant$84) | $10^{-8}$($\geqslant 10^{-8}$) |
| SMA2-W | 40 (25–65) | 3.2 (2.2–4.5) | $1.0 \times 10^6$ ($6.3 \times 10^4$—$2.5 \times 10^6$) | 64.0 (63–70) | $10^{-7}$($\geqslant 10^{-8}$) |
| SMA4 | 45 (30–90) | 3.6 (0.8–7.9) | $5.6 \times 10^4$ ($10^3$–$6.3 \times 10^5$) | 99.9 ($\geqslant$20) | $10^{-7}$($10^{-6}$–$10^{-9}$) |

**Note.** The 1$\sigma$ confidence intervals are indicated in parentheses.

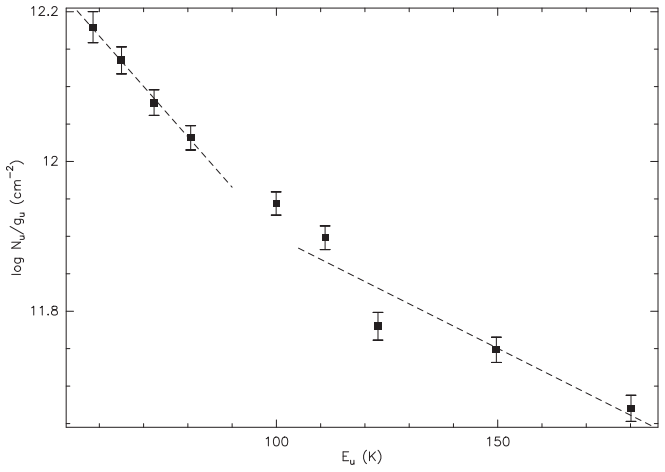


**Figure 13.** Population diagram for $SO_2$ at the SMA1 emission peak.

state DCN/HCN abundance ratio, but this looks less probable. In principle, interiors of the accretion disk can be well shielded from an external radiation, probably providing necessary low temperatures. In any case this clump deserves further investigation in order to clarify its properties and nature. It is worth mentioning that the mass of this clump cannot be lower than $\sim 1\ M_\odot$, otherwise the inferred $^{13}CS$ abundance would be unrealistically high. The virial mass we estimate about the same, hence the clump can be gravitationally bound.

### 4.2. SMA2

As in case of the SMA1 the spectral slope for the continuum emission in the frequency range 284–350 GHz is too low ($\sim$1.3), which is probably caused by a higher flux loss at higher frequencies. With the SMA at sub-arcsecond resolution we detected a compact component in the continuum emission of about the same size as in the SMA1. However, no high-excitation molecular lines could be detected in this area. In Paper I we derived the temperature of the SMA2 clump $\sim$40 K. Now with the extended data set, from the methanol excitation analysis (Section 3.1.1) we found the 1$\sigma$ confidence interval for temperatures of 40–80 K (Table 8). The best estimate of the methanol relative abundance is $X(CH_3OH) \sim 10^{-8}$. These estimates are obtained at the 2 arcsec scale. It cannot be excluded that the temperature of the compact structure observed in the very extended configuration is somewhat higher. However, it cannot be much higher since there is no sign of a higher temperature component in the molecular data. Assuming a temperature of 50 K we obtain the mass of the compact core $\sim 0.2\ M_\odot$.

To the west from the SMA2 there is an area of molecular emission without a continuum counterpart in the SMA data, observed earlier in the $N_2H^+$, $NH_3$, and several $CH_3OH$ lines (Paper I and Wang et al. 2011). Our new methanol data analysis indicates a temperature in the range 25–65 K and a density $n(H_2)$ in the range $6.3 \times 10^4$–$2.5 \times 10^6$, $X(CH_3OH) \sim 10^{-7}$ (Table 8). Some of the methanol transitions are inverted in the model and can be masing. These high

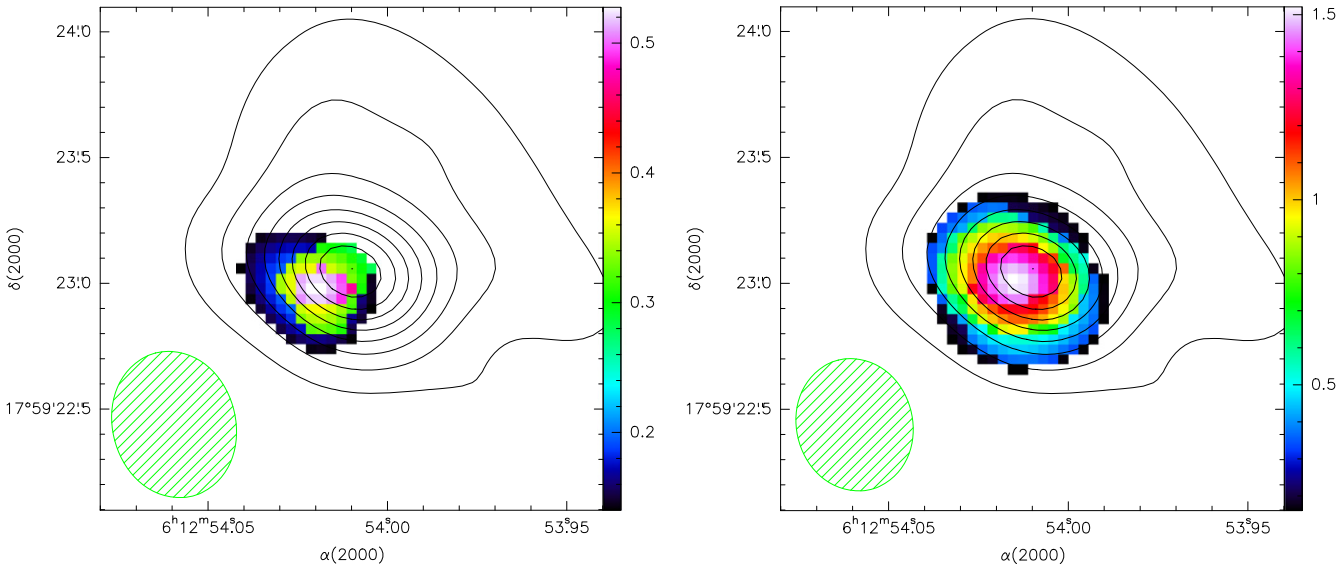


**Figure 14.** Maps of the integrated intensity of the DCN $J = 3$–2 (left panel) and $^{13}$CS $J = 5$–4 (right panel) transitions (color scale) toward the SMA1 clump. The intensity units are Jy beam$^{-1}$ km s$^{-1}$. The beam size is 0.″4. The contours show the 1.3 mm continuum emission with the same angular resolution. The beam for the molecular maps is shown in the lower left corner of both panels.

gas densities and rather high methanol abundances at relatively low temperatures can be explained by the influence of shock.

### 4.3. SMA3

In Paper I we did not detect this component which coincides with the near-infrared source NIRS 1 (Tamura et al. 1991) and is identified as a massive disk candidate by NIR polarization observations (Jiang et al. 2008). However, Simpson et al. (2009) argued that these measurements could be affected by instrumental effects and there is no real evidence for the "polarization disk" here. At the same time the NIR measurements indicate a possible outflow related to this object. A comparison with the measurements by Wang et al. (2011) gives a spectral index of about 3.3 in the frequency range 225–350 GHz, consistent with the optically thin dust emission. Wang et al. (2011) estimated the mass of this clump at about 2 $M_{\odot}$. At sub-arcsecond resolution we do not see any continuum (Figure 1) or molecular emission at this position.

### 4.4. SMA4

This clump was first detected in Paper I. It shows a weak continuum and spectral line emission in several molecular transitions. The measured continuum flux density at 350 GHz is practically the same as at 284 GHz which also implies a much higher flux loss at the higher frequency. The temperature derived from our new methanol data analysis is about 45 K (Table 8), higher than estimated in Paper I from ammonia data. However, the ammonia emission here is very weak and the uncertainties are high. Some methanol transitions are inverted in the model. The influence of shock is also probable.

## 5. MORPHOLOGY AND PROPERTIES OF THE OUTFLOWS

In the S255IR area high velocity emission is detected in lines of CO, SiO and several high density tracers including HCN, HCO$^+$, and CS. In Figures 15, 16 we present channel maps of the CO $J = 3$–2 emission in the blue and red line wings, respectively. The maps of the integrated line wing emission (Figure 17) show that the CO high velocity emission observed with the SMA looks like a highly collimated bipolar outflow originating near SMA2. There is another more compact component near SMA1.

On the other hand the bipolar outflow observed in HCN and HCO$^+$ is apparently associated with SMA1 while is parallel to the CO flow (Figure 17). It is apparently associated with the jet observed in particular in the Fe II emission which is also plotted in this figure. It is worth mentioning that the extent of the jet is much smaller than the extent of the outflow seen in CO, although their orientations coincide.

The SMA data alone hint at two parallel outflows with different origins. However, single-dish CO(3–2) observations with the IRAM 30 m telescope show a different picture. Here we see a wider outflow clearly originating at SMA1 (Figure 18). While the emission peaks coincide in the SMA and 30 m maps, near the driving source the CO emission measured with the SMA traces only the northern edge of the outflow. This shows that the SMA map gives a distorted picture and in reality we have here a wider angle outflow originating at SMA1.

Apparently this means that this northern edge of the outflow contains a relatively bright component with a characteristic scale comparable to the SMA beam. The southern edge of the outflow near the driving source would be more diffuse and resolved out by the SMA. Most probably this implies that the CO emission is formed in a compressed layer surrounding the outflow cavity. For some (unclear) reason in the northern part this layer is more pronounced. It is worth mentioning that the brightest peaks of the high velocity CO emission practically coincide in the SMA and 30 m maps and also coincide with spots of molecular hydrogen emission (Wang et al. 2011) which probably indicate bow shocks. Basic physical parameters of the outflow were estimated by Wang et al. (2011) from their CO(2–1) data. Our new data are consistent with these estimates.

The position–velocity (P–V) diagram for the outflow along the cut indicated in Figure 18, constructed from the 30 m data, is shown in the left panel of Figure 19. The gap at $V_{\rm LSR} \sim 24$ km s$^{-1}$ is caused by the emission at the reference offset

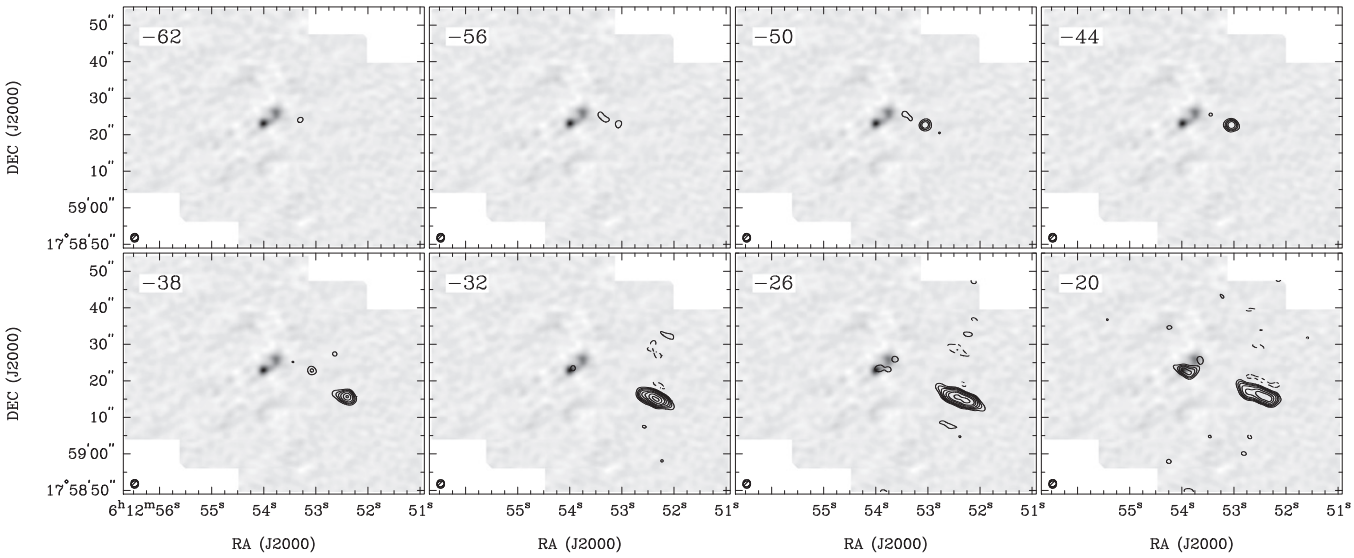


**Figure 15.** Channel maps of the CO blue wing emission in the S255IR. The numbers in the upper left corner indicate the channel velocity in km s$^{-1}$. The dashed contours show negative features due to the missing flux. The contour levels are (−3, 3, 5, 7, 10, 15, 20, 30, 40) × 100 mJy beam$^{-1}$. The SMA beam is shown in the lower left corner of each panel.

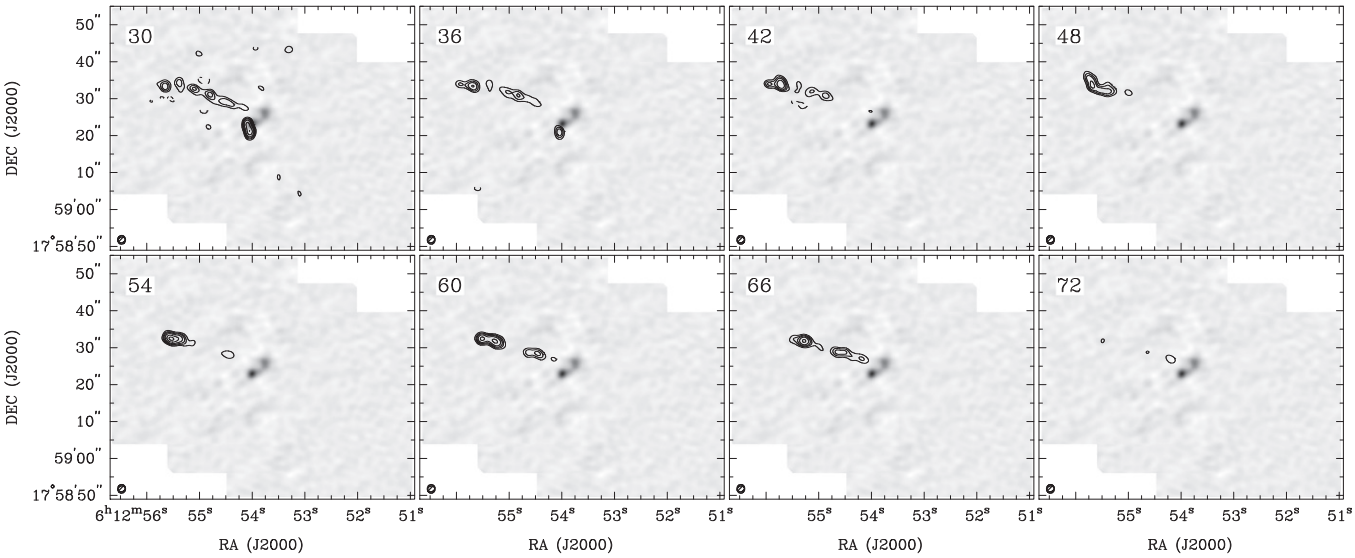


**Figure 16.** Channel maps of the CO red wing emission in the S255IR. The numbers in the upper left corner indicate the channel velocity in km s$^{-1}$. The dashed contours show negative features due to the missing flux. The contour levels are (−3, 3, 5, 7, 10, 15, 20, 30, 40) × 100 mJy beam$^{-1}$. The SMA beam is shown in the lower left corner of each panel.

position mentioned above. In the right panel we present the P–V diagram obtained from the SMA CO(3–2) data. The main features of these diagrams coincide. They show non-monotonic dependence of the velocity on offset, which hints at two outflow components at different distances from the driving source. These P–V diagrams are somewhat different from that presented by Wang et al. (2011). However, Wang et al. (2011) plotted this diagram for a different cut, with the position angle of 75°, which makes the direct comparison irrelevant.

In Figure 20 we plot the P–V diagram for the $HCO^+$(4–3) emission as observed with the SMA, along with the part of the CO(3–2) P–V diagram for the same intervals of the offset and velocity. The diagrams are very similar, which means that both molecules trace apparently the same gas.

### 5.1. Dense High Velocity Clump

Our data show a strong, compact blue-shifted CS and HCN emission close to the peak of the CO blue-shifted line wing emission. The peak of this CS and HCN emission is marked by cross in Figure 18. The CO(3–2), CO(2–1), HCN(4–3), CS(7–6), $HCO^+$(4–3), and $N_2H^+$(3–2) spectra toward this position are presented in Figure 21.

One can see rather strong and broad HCN and CS lines at a central velocity of about −5 km s$^{-1}$. There is a hint of wings in these lines extending to about −20 km s$^{-1}$. The peak of the CO emission, especially in the higher $J = 3$–2 transition is observed at more negative velocities. There is no detectable $HCO^+$(4–3), $N_2H^+$(3–2), $CH_3CN$, and continuum emission (for $N_2H^+$ and $CH_3CN$ we use the data from Paper I).

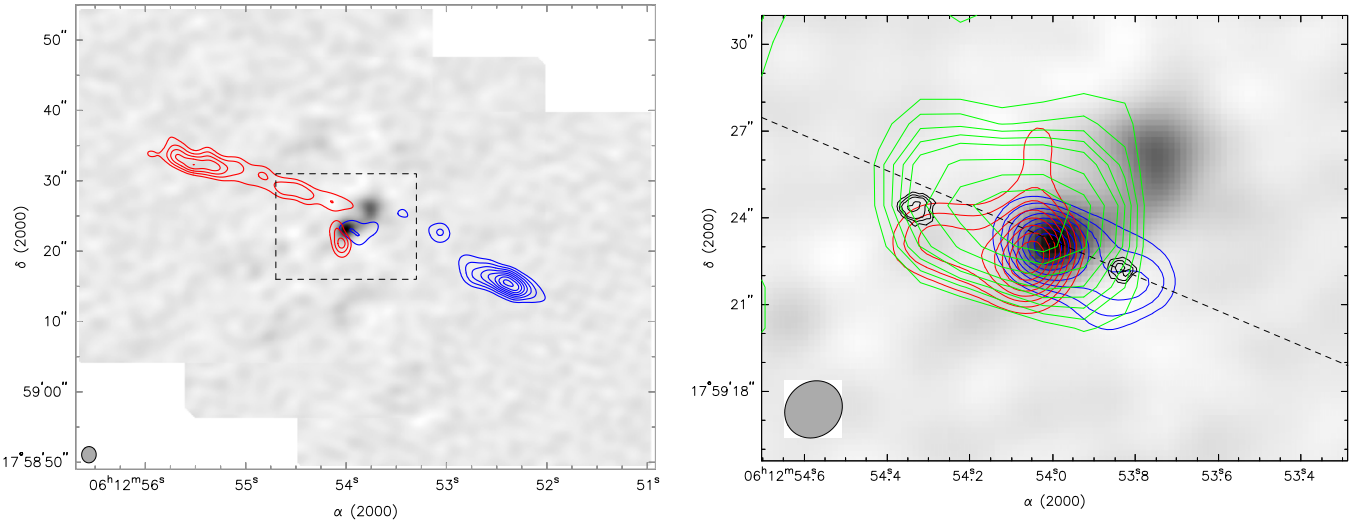


**Figure 17.** Left panel: maps of the CO(3–2) high velocity emission as observed with the SMA (blue and red contours) in the S255IR area overlaid on the continuum image at 0.8 mm. The SMA1 and SMA2 continuum clumps are marked. The velocity intervals are from −63 to −13 km s$^{-1}$ for the blue wing and from 25 to 75 km s$^{-1}$ for the red wing. The dashed rectangle indicates the area shown in the right panel. Right panel: maps of the $HCO^+$(4–3) high velocity emission (blue and red contours) in the S255IR area overlaid on the continuum image at 0.8 mm. The velocity intervals are from −19 to 3 km s$^{-1}$ for the blue wing and from 11 to 27 km s$^{-1}$ for the red wing. The black contours show the Fe II emission (Wang et al. 2011). The map of the 15 GHz continuum emission (from the VLA archival data, the angular resolution is about 4 arcsec) is plotted with green contours. The dashed line indicates the jet axis (P.A .= 67°) as in Figure 5. The SMA beam is shown in the lower left corner of both panels.

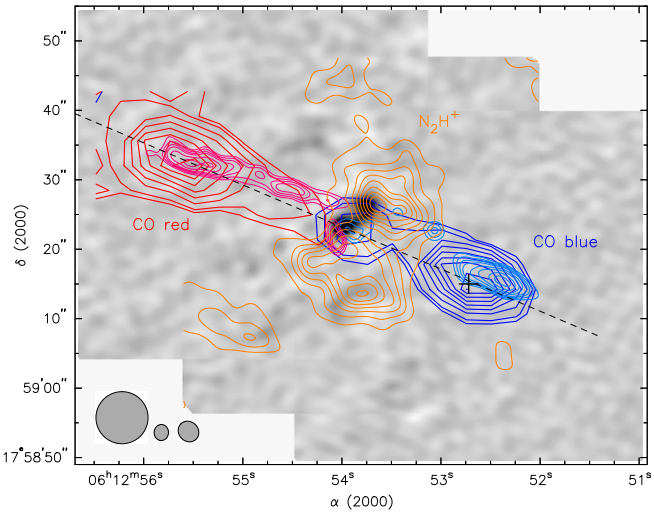


**Figure 18.** Maps of the CO(3–2) high velocity emission as observed with the IRAM 30 m telescope (blue and red thick contours) in the S255IR area overlaid on the continuum image at 0.8 mm. The thin contours show the SMA maps from Figure 17. The dashed line indicates the axis of the position–velocity cut (P.A. = 67°). The orange contours show the $N_2H^+$(3–2) integrated line emission obtained by combining the SMA and 30 m data. The cross marks the position of the high-velocity dense clump (Section 5.1). The 30 m beam and the SMA beams for the CO and $N_2H^+$ observations, respectively, are shown in the lower left corner (from left to right).

The spatial distribution of the CS(7–6) and CO(3–2) emission integrated in the velocity ranges −13…+1 km s$^{-1}$ and −19…+1 km s$^{-1}$, respectively, is shown in Figure 22. The HCN distribution is very similar to that of CS. The deconvolved size of the CS emitting clump is about $1\farcs1 \times 0\farcs3$ which corresponds to 1800 AU × 500 AU. It is apparently located at the head of the stream observed in CO, almost exactly at the jet axis shown in Figure 18.

At the velocity of the CS and HCN emission peak, the brightness temperatures in the CO(3–2), CO(2–1), and HCN(4–3) lines are practically the same. The frequencies of the CO(3–2), HCN(4–3), and CS(7–6) lines are close to each other and beam parameters for them should be similar, too. However, the comparison with the CO(2–1) is complicated by the significantly different frequencies.

The CO(3–2) line is most probably saturated. Then the HCN(4–3) line should be saturated, too. The CS line is weaker implying either a relatively lower optical depth (but close to unity anyway) or a smaller size of the emission region. A simple modeling using, e.g., RADEX (van der Tak et al. 2007) shows that the column densities of HCN and CS required to explain such optical depths are $\gtrsim 10^{15}$ cm$^{-2}$. The relative abundances of these molecules are $\leqslant 10^{-8}$. Therefore the total gas column density in the clump is $\gtrsim 10^{23}$ cm$^{-2}$. Then, using the size estimated above we obtain the gas density $n \gtrsim 3\times 10^6$ cm$^{-3}$. This estimate is consistent with the observations of the HCN and CS lines which require at least such densities for excitation.

The large HCN and CS line widths indicate that the clump is gravitationally unbound. The virial mass of this clump estimated in the usual way (e.g., Zinchenko et al. 1994) is $M_{\rm vir} \sim 30\,M_\odot$. At the same time, the non-detection of dust emission implies an upper limit for mass orders of magnitudes lower. Therefore, the clump represents a transient entity.

It is worth mentioning the non-detection of $HCO^+$ and $N_2H^+$ emission. Both molecules can be destroyed by dissociative recombination (e.g., Zinchenko et al. 2009). Therefore their absence can indicate an enhanced ionization in the dense clump.

### 5.2. Ionized Gas

In Figure 17 we plot the map of the 15 GHz continuum emission near the SMA1/SMA2 clumps (from the VLA archival data, the angular resolution is about 4 arcsec) which shows the distribution of the ionized gas in this area. This ionized component seems to be associated with the jet traced in the Fe II emission. The GMRT map at 1280 MHz looks similar but there is a significant positional uncertainty in the GMRT

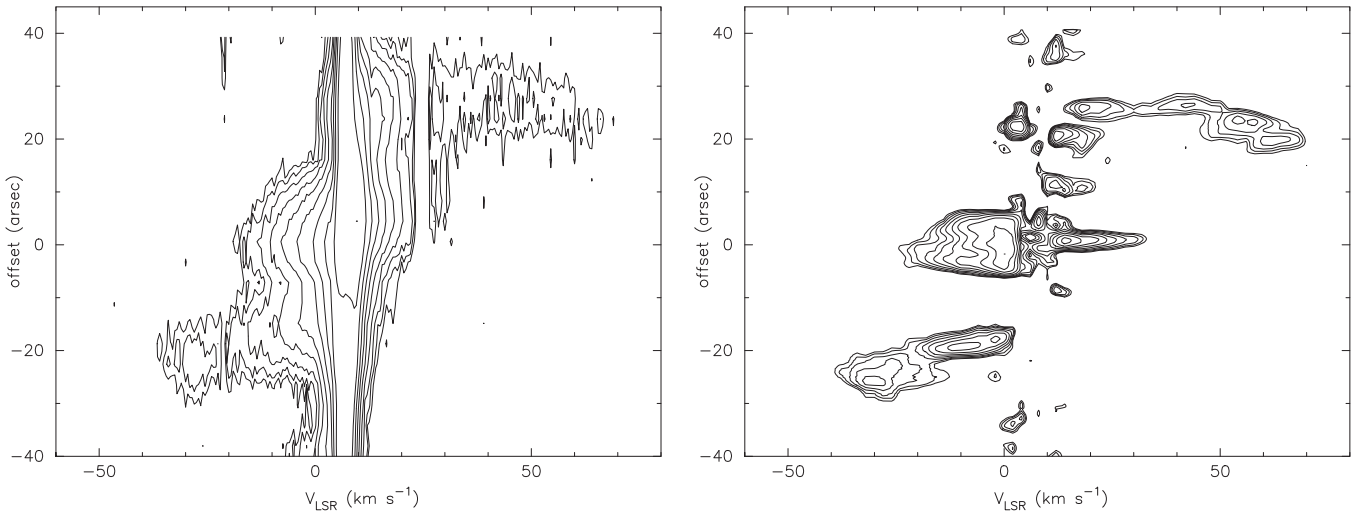


**Figure 19.** Left panel: the position–velocity map for the CO(3–2) emission as observed with the IRAM 30 m telescope along the cut indicated in Figure 18. The contour levels are on a logarithmic scale from 0.4 to 31.5 K. The gap at $V_{\rm LSR} \sim 24$ km s$^{-1}$ is caused by the emission at the reference offset position mentioned above. Right panel: the position–velocity map for the CO(3–2) emission as observed with the SMA along the same cut. The contour levels are on a logarithmic scale from 0.5 to 11.5 Jy beam$^{-1}$.

data (Paper I). Properties of the continuum source were estimated in Paper I and by Ojha et al. (2011). The emission measure is EM $\sim$ (1–2.5) $\times$ 10$^7$ pc cm$^{-6}$. Taking into account the observed size of the continuum source, the electron density is $n \sim 3 \times 10^4$ cm$^{-3}$.

## 6. SURROUNDINGS

The surroundings of the SMA1/SMA2 clumps and high-velocity outflow are traced in several molecular lines. One of the most informative is the $N_2H^+$(3–2) transition observed with both the SMA and the IRAM 30 m telescope. The combined map of the $N_2H^+$(3–2) emission is presented in Figure 18. It shows an absence of $N_2H^+$ in the hot core in accordance with our previous findings (Paper I). The overall morphology of the $N_2H^+$ emission suggests that it originates in an envelope around the central cores and the outflow lobes.

The distribution of the SiO(5–4) emission is different (Figure 23). It peaks near the SMA1 core. There is also a feature in the area of the blue outflow lobe that may be associated with the $N_2H^+$ emission. The CS(7–6) distribution (right panel in Figure 23) seems to be the most uniform one. It shows a rather smooth, almost spherical halo around the SMA1 and SMA2 cores. There is no sign of the outflow influence on the CS distribution. One may suspect that the optical depth in the CS line is too high and we see only the outer regions of the core. However, the SMA1 and SMA2 clumps are well resolved in this map which makes such explanation less probable. Then, the total gas distribution is apparently not significantly affected, too.

## 7. DISCUSSION

The main goal of this study is the characterization of the outflow and probable accretion disk associated with the massive YSO in the S255IR clump. The data presented in the previous sections shed new light on this system.

Concerning the outflow, one of the main findings is that the SMA interferometric data alone give a rather distorted picture. They hint at two highly collimated parallel outflows with different centers of origin. However, this impression is apparently caused by a significant flux loss in the interferometric measurements. The single-dish CO observations clearly show a single less collimated outflow originating at the SMA1 core. The CO emission retrieved by the SMA near the driving source originates apparently from the northern wall of the outflow cavity. This means that this part of the wall is rather thin and bright. The absence of a noticeable CO emission at the opposite side of the wall implies a more diffuse distribution of the emission here, probably due to the density structure of the surrounding medium.

The question arises of how common this effect is in interferometric studies of outflows. We can easily imagine a situation when an interferometric image will show multiple outflows from a single driving source, while in fact there is a single wide-angle outflow.

The observed P–V diagrams for the outflow (Figures 19, 20) most probably indicate periodic ejections from the driving source. Two events can be traced in the data. They apparently created jet knots at different distances from the central star. The older one is responsible for the extended CO outflow. The peaks of the CO emission coincide with bright $H_2$ emission spots (Wang et al. 2011) which probably indicate bow shocks at the heads of the jets. The next ejection event created other bow shocks which are seen in particular in the Fe II emission (Figure 17). This later ejection entrains dense molecular gas observed in the wings of the $HCO^+$, HCN and CS lines. It is also traced in the CO emission as can be seen in the CO position–velocity diagram (Figures 19, 20). Another manifestation of this activity is apparently the dense high velocity clump (Section 5.1), which most probably represents dense gas at the head of a bow shock. All the jet knots lay practically on a straight line. Therefore the orientation of the jet does not change significantly with time. The age of the first, extended outflow was estimated at about 7000 years by Wang et al. (2011). Assuming the same ejection velocities for the two events and comparing distances of the bow shocks from the driving source we can conclude that the second ejection happened about 1000 years ago. Therefore the time interval between the ejection events is about 6000 years (the age

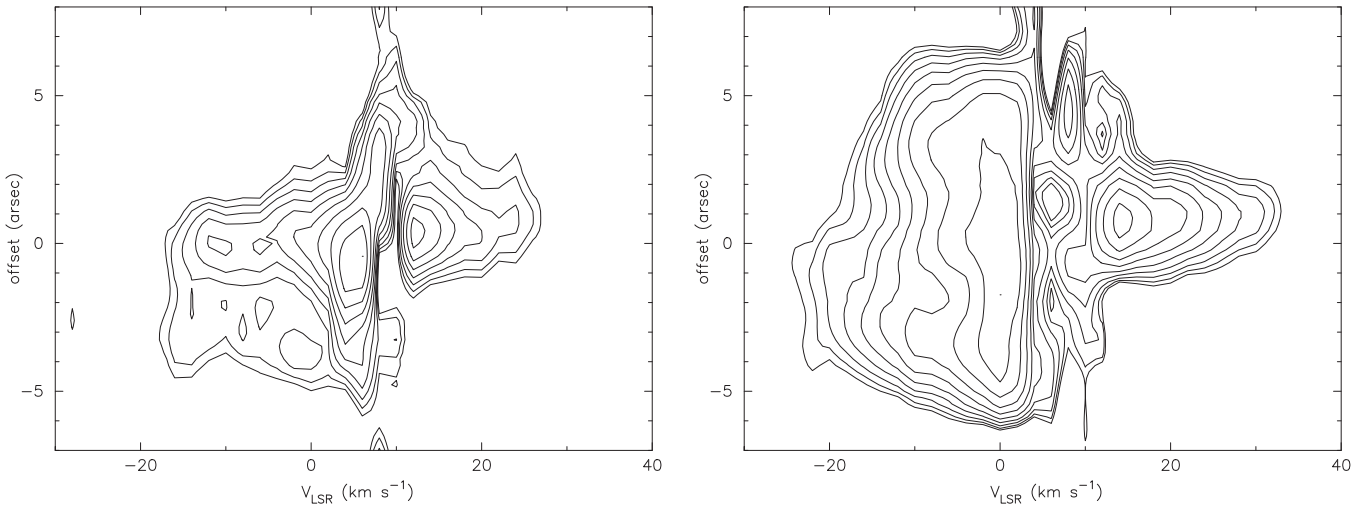


**Figure 20.** Left panel: the position–velocity map for the $HCO^+$(4–3) emission as observed with the SMA along the cut indicated in Figure 17. The contour levels are on a logarithmic scale from 0.4 to 7.6 Jy beam$^{-1}$. Right panel: a part of the position–velocity map for the CO(3–2) emission measured by the SMA from Figure 19 for the same intervals of the offset and velocity as in the left panel.

estimates were done under the usual assumption of an inclination angle for a jet of 45°).

Several entrainment mechanisms are usually discussed for molecular outflows (e.g., Arce et al. 2007; Frank et al. 2014). In our case the most probable one is the jet bow-shock model (e.g., Raga & Cabrit 1993). The main argument in favor of this model is the obvious presence of several bow shocks (traced in the $H_2$ and Fe II emission) clearly associated with the high-velocity molecular gas. This model is also consistent with the observed outflow morphology and kinematics. The shape of the P–V diagram differs from the frequently observed "Hubble law" and shows a range of velocities at the largest distances from the driving source. A similar shape was observed in some other outflows which are apparently driven by bow shocks and this type of shape is expected in the theoretical models (e.g., Lee et al. 2000).

The jet is apparently launched from the accretion disk around the central massive young star. As mentioned above, there is a chain of water masers along the jet. For several water maser spots shown in Figure 5, proper motions have been measured (Goddi et al. 2007). The velocities (from ∼10 to ∼30 km s$^{-1}$ at a distance of 1.6 kpc) are mostly perpendicular to the jet axis with outward components in some cases. The maser velocity pattern is consistent with clockwise rotation around the core center. Velocities of the masers closest to the center imply a dynamical mass of the order of 20 $M_\odot$. The mass of the central star is estimated to be 27 $M_\odot$ (Ojha et al. 2011) assuming a distance of 2.5 kpc. At a distance of 1.6 kpc the mass of the star would be $23.5 \pm 3.6\ M_\odot$. This estimate is based on the unpublished value of the star luminosity of $(6.8 \pm 2.8) \times 10^4\ L_\odot$ (for the distance of 1.6 kpc). Now we reconsidered the star SED by including data at millimeter wavelengths from Zinchenko et al. (2009). This results in the luminosity of $(3.5 \pm 0.3) \times 10^4\ L_\odot$ and mass of $20 \pm 2\ M_\odot$. It is worth mentioning that Pashchenko et al. (2003) estimated the mass of the central star to be (6–7) $M_\odot$ from their analysis of water maser variability. However, they employed a systemic velocity of 8.3 km s$^{-1}$ that contradicts our findings which clearly show the systemic velocity to be about 4.8 km s$^{-1}$. In the following we will take the mass of 20 $M_\odot$ as the most probable value. This is sufficient to explain velocities of the masers closest to the star. However, maser spots located at larger distances from the center have similar velocities and imply a much larger central mass of the order of 100 $M_\odot$. This value is inconsistent with all other estimates. The corresponding mean density would be unrealistically high. This means that we probably need another explanation for the maser velocities. One speculation is that it might be jet rotation. Rapid rotation of protostellar jets is expected in theoretical models (e.g., Pudritz et al. 2007) and was indeed observed in some cases (Bacciotti et al. 2002).

Water masers are thought to be excited by interaction of the jet with the surrounding medium. The fact that they are moving in one direction on each side of the central star implies some asymmetry in the system. There may be some misalignment between the jet and the rotation axis of the material in the outer parts of the clump (apparently, in the axially symmetric case the observed maser movements would be symmetric relative to the axis). It can be that in the inner part the orientation of the disk plane is different. However, the difference cannot be large. We see also other indications of the jet interaction with the surrounding medium, in particular, increased line widths along the jet.

Figure 5 shows that the water maser condensations are shifted from the jet axis in direction of their proper motion. This projected shift is of the order of 200 AU. At the velocities mentioned above, the maser condensations would travel this distance in about 30–100 years. From this consideration it looks probable that the event that created these masers happened quite recently.

The disk is apparently strongly fragmented as follows from the derived beam filling factor (∼0.2) for $CH_3CN$ and $CH_3OH$. The mean gas density in the disk is about $6 \times 10^8$ cm$^{-3}$. The density of the fragments should be much higher. Observations of vibrationally excited HCN indicate densities $>10^{10}$ cm$^{-3}$ which is consistent with this picture.

The derived mass of the hot gas (∼0.3 $M_\odot$) is an order of magnitude insufficient to gravitationally bind the core. The virial mass estimated in the usual way (e.g., Zinchenko et al. 1994) from the line width is about 7 $M_\odot$. There can be also some amount of cold material in the disk, as follows from the DCN observations. However, the total mass of the disk is apparently much lower than the mass of the central star which is estimated to be about 20 $M_\odot$ (see above). Since the disk mass is significantly lower than the star mass, the disk is probably not self-gravitating and we may expect Keplerian rotation.

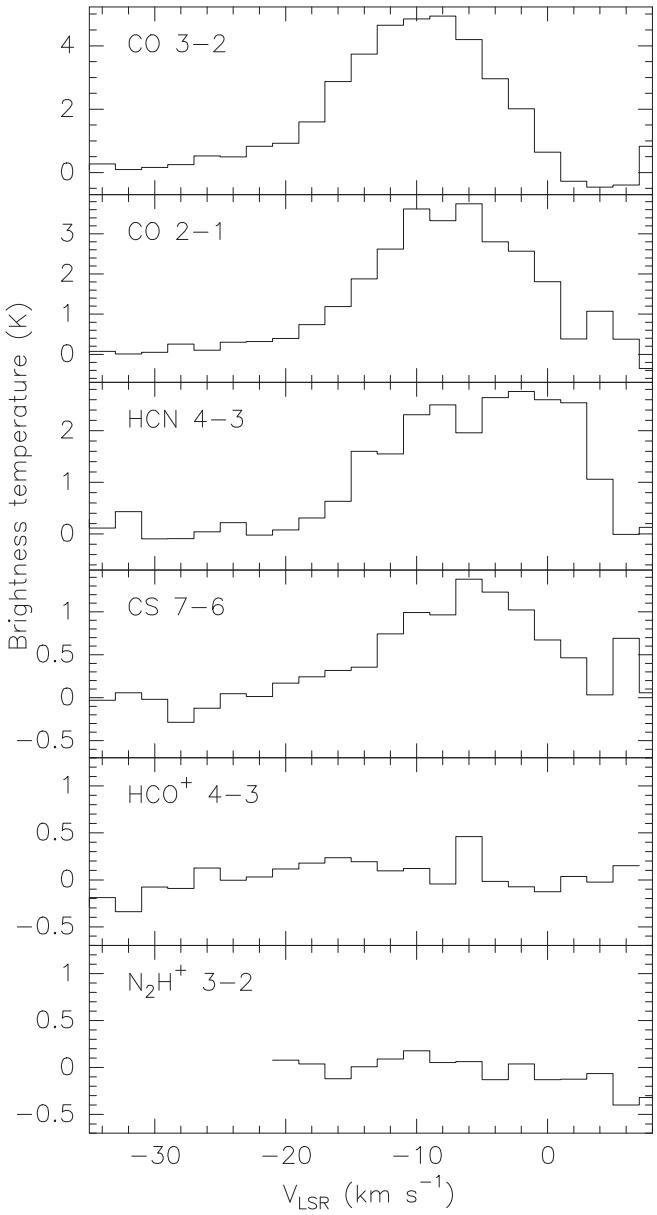


**Figure 21.** CO(3–2), CO(2–1), HCN(4–3), CS(7–6), $HCO^+$(4–3), and $N_2H^+$(3–2) spectra toward the position marked by cross in Figure 18.

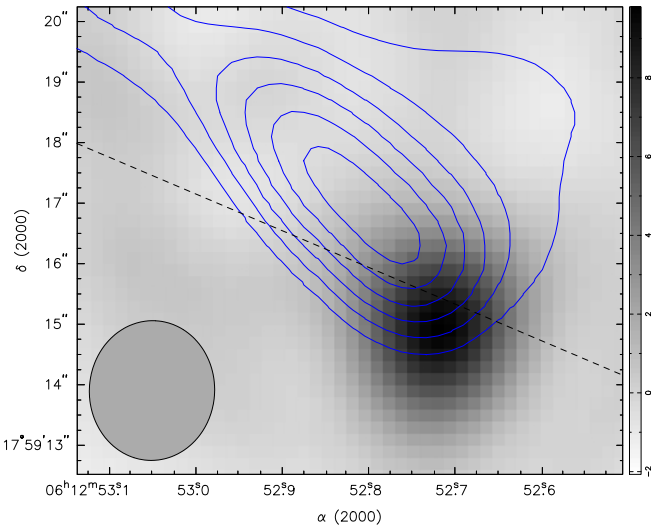


**Figure 22.** Map of CO(3–2) emission in the velocity range $-19\ldots+1$ km s$^{-1}$ (contours) overlaid on an image of CS(7–6) emission in the velocity range $-13\ldots+1$ km s$^{-1}$ (gray scale). The intensity units for the image are Jy beam$^{-1}$ km s$^{-1}$. The contour levels are (3, 5, 7, 9, 11, 13) × 5 Jy beam$^{-1}$ km s$^{-1}$. The SMA beam is shown in the lower left corner.

Unfortunately the achieved angular resolution is not sufficient to reliably measure the disk rotation curve.

For a central mass of 20 $M_\odot$ the inclination angle of the disk (derived from a comparison of the observed rotation line-of-sight velocity with the expected velocity for this mass) should be small, about 25° (Figure 6), i.e., the disk is seen almost face-on. This is consistent with our maps which do not show a significant elongation of this object. However, this conclusion looks somewhat suspicious because of the well-collimated appearance of the molecular outflow. Observations at a higher angular resolution are needed to clarify the structure and kinematics of this object.

The temperature of the hot gas derived from the $CH_3CN$, $CH_3OH$, and $SO_2$ observations is about 130–180 K. A similar estimate for the temperature of the hot component was obtained by us many years ago from the analysis of the IRAS data (Zinchenko et al. 1990). The HNCO rotational temperature is somewhat higher, about 320 K. However, as mentioned above, this value probably represents an upper limit to the excitation temperature. In addition, the HNCO excitation can be influenced by the FIR radiation. The HNCO excitation in massive cores was discussed by Zinchenko et al. (2000). That analysis shows that in the present case collisional excitation can be effective. The critical density for excitation of the $K_{-1} = 3$ ladder is of the order of $10^{10}$ cm$^{-3}$. Such density is quite possible in the SMA1 core as follows from the estimates above. However, radiative excitation by FIR emission via the *b*-type transitions cannot be excluded. With a column density of $N(H_2) \sim 3\times 10^{24}$ cm$^{-2}$ the dust will be optically thick at these frequencies creating a sufficiently strong radiation field. The HNCO excitation especially in the higher $K_{-1}$ ladders may reflect the effective temperature of this field.

The highest temperature of the observed molecular material is about 300 K. Taking the source luminosity to be about $3.5 \times 10^4\, L_\odot$ (see above) this value corresponds to the dust equilibrium temperature at a distance of 200–300 AU from the star. Since we do not see warmer molecular gas, no dust should be present within this radius in a case of no shielding. However, this radius is comparable to the observed size of the core and we do not see any central hole in the molecular distribution. It is then possible that shielded molecular clumps are distributed at smaller radii.

In this respect an interesting feature of our observations is the apparently relatively cold and rather massive clump with a strong DCN emission. It may be gravitationally bound and the mass of the clump is sufficiently high to consider it as a possible low-mass protostar.

Concerning the surroundings of the SMA1 clump, we see that the outflow strongly affects the chemical composition of the medium. The $N_2H^+$ molecules are destroyed along the outflow. The SiO distribution also seems to be significantly affected. At the same time there is no noticeable influence on the CS distribution. The density structure is probably not affected either. As mentioned above (Sections 4.2, 4.4) the

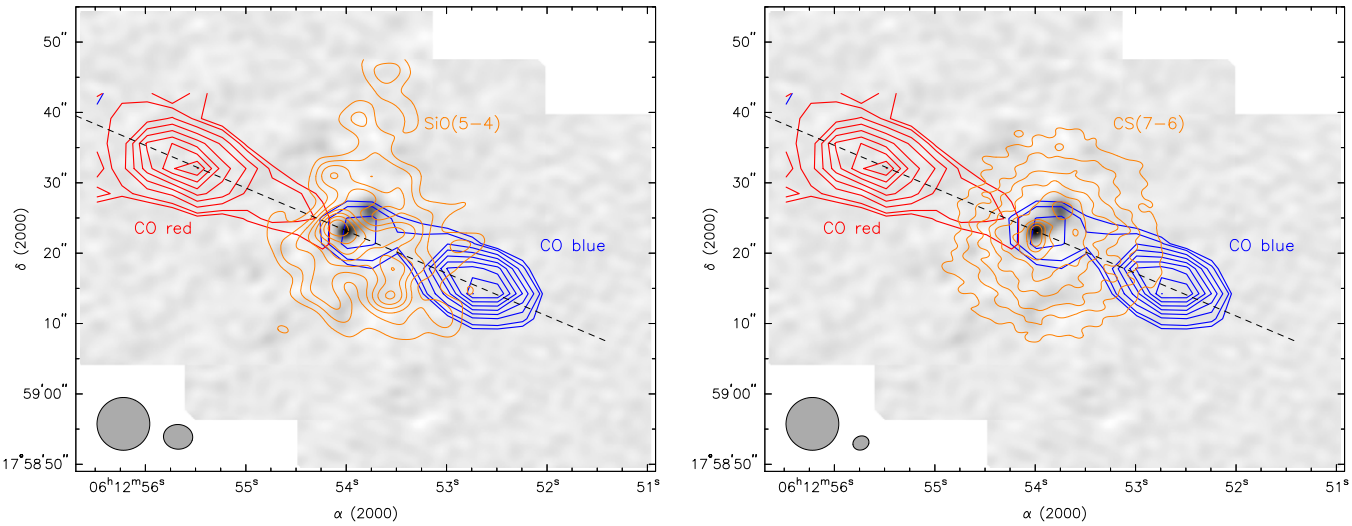


**Figure 23.** Left panel: the maps of the SiO(5–4) (left panel) and CS(7–6) (right panel) integrated line emission obtained by combining the SMA and 30 m data (orange contours) overlaid on the continuum image at 0.8 mm. The maps of the CO(3–2) high velocity emission as observed with the IRAM 30 m telescope (blue and red thick contours) from Figure 18 are also shown. The beams for the IRAM 30 m telescope and for the combined maps are shown in the lower left corner of each panel.

nearby clumps are probably influenced by shocks that are apparently associated with this outflow.

## 8. CONCLUSIONS

We presented the results of our observations of the S255IR area with the SMA at 1.3 mm in the very extended configuration and at 0.8 mm in the compact configuration as well as with the IRAM 30 m at 0.8 mm. The best achieved angular resolution is about 0.4 arcsec. The dust continuum emission and several tens of molecular spectral lines are observed. The majority of the lines is detected only toward the S255IR-SMA1 clump. In summary, our main findings are the following.

1. The S255IR-SMA1 clump apparently represents a rotating structure (probably a disk) around the young massive star. The achieved angular resolution is still insufficient to establish the character (Keplerian or non-Keplerian) of the rotation. The temperature of the molecular gas reaches 130–180 K. The size of the clump is about 500 AU. It is apparently strongly fragmented as follows from the derived small (∼0.2) beam filling factors for various molecules. The mean gas density is about $6 \times 10^8$ cm$^{-3}$. The density of the fragments should be much higher which is confirmed by observations of HNCO and vibrationally excited HCN. The mass of the hot gas is ∼0.3 $M_\odot$ and the total mass of the clump is significantly lower than the mass of the central star (about 20 $M_\odot$). The inclination angle of the disk (derived from comparison of the observed rotation line-of-sight velocity with the expected rotation velocity for this mass) should be small, about 25°.
2. We detected a strong DCN(3–2) emission near the center of the SMA1 clump. Most probably it indicates the presence of a rather large amount ($\gtrsim$1 $M_\odot$) of cold ($\leqslant$80 K) material. This cold clump can be gravitationally bound.
3. High velocity emission is observed in the CO line as well as in lines of high-density tracers HCN, HCO$^+$, CS, and other molecules. The CO outflow is much more extended than that observed in the lines of high-density tracers. Its morphology obtained from a combination of the SMA and IRAM 30 m data is significantly different from that derived from the SMA data alone. The CO emission detected with the SMA traces only one boundary of the outflow and leads to a rather distorted picture of the outflow structure. The velocity of the CO outflow reaches ∼60 km s$^{-1}$.
4. The outflow is most probably driven by the jet bow shock mechanism. The available data indicate at least two major ejection events with a time interval of several thousand years between them. The direction of the ejections does not change with time. The high-velocity emission in the lines of high-density tracers is associated with the peaks of the Fe II emission related to the bow shocks caused by rather recent ejections from the SMA1.

   We detected a dense high-velocity clump apparently associated with one of the bow shocks. It shows a strong emission in the HCN(4–3) and CS(7–6) lines. At the same time there is no detectable HCO$^+$(4–3) or $N_2H^+$(3–2) emission which can be probably explained by enhanced ionization.
5. The proper motions of the water masers excited along the jet imply some misalignment of the jet with the rotation axis of the material in the outer parts of the clump. It could be that the orientation of the disk in the inner and outer parts is somewhat different. However, the difference cannot be large.
6. The outflow strongly affects the chemical composition of the surrounding medium. The $N_2H^+$ molecules are destroyed along the outflow. The SiO distribution also seems to be significantly affected. At the same time there is no sign of the outflow's influence on the CS distribution. The total gas distribution is apparently not significantly affected either.

This work was supported by the Russian Academy of Sciences (Research program No. 17 of the Department of Physical Sciences), the Russian Foundation for Basic Research (RFBR), the Ministry of Science and Technology (MoST) in

Taiwan, and the Department of Science and Technology (DST) of the Government of India in the frameworks of the research grants RFBR 08-02-92001-NSC, RFBR 13-02-92697-Ind, RFBR 15-02-06098, 15-52-45057, and DST-RFBR INT/RUS/RFBR/P-142. S.-Y.L. and Y.-N.S. acknowledge grant support 102-2119-M-001-010-MY2 from MoST. A.M.S. was supported by the Russian Science Foundation (grant No. 15-12-10017). S.V.S. was supported by the Ministry of Education and Science of the Russian Federation (state task No. 3.1781.2014/K). Y.W. was supported by the Swiss National Science Foundation, NSFC 11303097 and 11203081, China. The research is also partly supported by the grant within agreement No. 02.B.49.21.0003 between The Ministry of Education and Science of the Russian Federation and Lobachevsky State University of Nizhni Novgorod and by the Russian Education and Science Ministry Project 3.1252.2014/k. We are grateful to Elena Trofimova for help with line identification and to the anonymous referee for detailed helpful comments. The research has made use of the SIMBAD database, operated by CDS, Strasbourg, France.

## REFERENCES

Albertsson, T., Semenov, D. A., Vasyunin, A. I., Henning, T., & Herbst, E. 2013, ApJS, 207, 27
Arce, H. G., Shepherd, D., Gueth, F., et al. 2007, Protostars and Planets V, ed. B. Reipurth, D. Jewitt, & K. Keil (Tuscon, AZ: Univ. Arizona Press), 245
Bacciotti, F., Ray, T. P., Mundt, R., Eislöffel, J., & Solf, J. 2002, ApJ, 576, 222
Beuther, H., Walsh, A. J., & Longmore, S. N. 2009, ApJS, 184, 366
Boucher, D., Burie, J., Bauer, A., Dubrulle, A., & Demaison, J. 1980, JPCRD, 9, 659
Chavarría, L. A., Allen, L. E., Hora, J. L., Brunt, C. M., & Fazio, G. G. 2008, ApJ, 682, 445
Cragg, D. M., Sobolev, A. M., & Godfrey, P. D. 2005, MNRAS, 360, 533
Frank, A., Ray, T. P., Cabrit, S., et al. 2014, Protostars and Planets VI, ed. H. Beuther (Tuscon, AZ: Univ. Arizona Press), 451
Goddi, C., Moscadelli, L., Sanna, A., Cesaroni, R., & Minier, V. 2007, A&A, 461, 1027
Howard, E. M., Pipher, J. L., & Forrest, W. J. 1997, ApJ, 481, 327
Itoh, Y., Tamura, M., Suto, H., et al. 2001, PASJ, 53, 495
Jiang, Z., Tamura, M., Hoare, M. G., et al. 2008, ApJL, 673, L175
Lee, C.-F., Mundy, L. G., Reipurth, B., Ostriker, E. C., & Stone, J. M. 2000, ApJ, 542, 925
Miralles, M. P., Salas, L., Cruz-Gonzalez, I., & Kurtz, S. 1997, ApJ, 488, 749
Müller, H. S. P., Schlöder, F., Stutzki, J., & Winnewisser, G. 2005, JMoSt, 742, 215
Müller, H. S. P., Thorwirth, S., Roth, D. A., & Winnewisser, G. 2001, A&A, 370, L49
Ojha, D. K., Samal, M. R., Pandey, A. K., et al. 2011, ApJ, 738, 156
Ossenkopf, V. 1997, NewA, 2, 365
Ossenkopf, V., & Henning, T. 1994, A&A, 291, 943
Pashchenko, M. I., Lekht, E. E., & Tolmachev, A. M. 2003, AstL, 29, 26
Pickett, H. M., Poynter, R. L., Cohen, E. A., et al. 1998, JQSRT, 60, 883
Pirogov, L. E., & Zinchenko, I. I. 2008, ARep, 52, 963
Pirogov, L. E., Zinchenko, I. I., Johansson, L. E. B., & Yang, J. 2012, A&AT, 27, 475
Pudritz, R. E., Ouyed, R., Fendt, C., & Brandenburg, A. 2007, Protostars and Planets V, ed. B. Reipurth, D. Jewitt, & K. Keil (Tuscon, AZ: Univ. Arizona Press), 277
Raga, A., & Cabrit, S. 1993, A&A, 278, 267
Russeil, D., Adami, C., & Georgelin, Y. M. 2007, A&A, 470, 161
Rygl, K. L. J., Brunthaler, A., Reid, M. J., et al. 2010, A&A, 511, A2
Sault, R. J., Teuben, P. J., & Wright, M. C. H. 1995, in ASP Conf. Ser. 77, Astronomical Data Analysis Software and Systems IV, ed. R. A. Shaw, H. E. Payne, & J. J. E. Hayes (San Francisco, CA: ASP), 433
Scoville, N. Z., Carlstrom, J. E., Chandler, C. J., et al. 1993, PASP, 105, 1482
Sherwood, W. A., Arnold, E. M., & Schultz, G. V. 1980, in IAU Symp. 87, Interstellar Molecules, ed. B. H. Andrew, 133
Simpson, J. P., Burton, M. G., Colgan, S. W. J., et al. 2009, ApJ, 700, 1488
Snell, R. L., & Bally, J. 1986, ApJ, 303, 683
Sutton, E. C., Sobolev, A. M., Salii, S. V., et al. 2004, ApJ, 609, 231
Tamura, M., Gatley, I., Joyce, R. R., et al. 1991, ApJ, 378, 611
van der Tak, F. F. S., Black, J. H., Schöier, F. L., Jansen, D. J., & van Dishoeck, E. F. 2007, A&A, 468, 627
Veach, T. J., Groppi, C. E., & Hedden, A. 2013, ApJL, 765, L34
Wang, K.-S., Kuan, Y.-J., Liu, S.-Y., & Charnley, S. B. 2010, ApJ, 713, 1192
Wang, Y., Beuther, H., Bik, A., et al. 2011, A&A, 527, A32
Zinchenko, I., Caselli, P., & Pirogov, L. 2009, MNRAS, 395, 2234
Zinchenko, I., Forsstroem, V., Lapinov, A., & Mattila, K. 1994, A&A, 288, 601
Zinchenko, I., Henkel, C., & Mao, R. Q. 2000, A&A, 361, 1079
Zinchenko, I., Liu, S.-Y., Su, Y.-N., et al. 2012, ApJ, 755, 177
Zinchenko, I. I., Krasilnikov, A. A., Kukina, E. P., Lapinov, A. V., & Pirogov, L. E. 1990, SvA, 34, 458